IL NUOVO CIMENTO VOL. 9 A, N. 4 21 Giugno 1972

Precise Measurement of the Anomalous Magnetic Moment of the Muon.

J. BAILEY, W. BARTL (*), G. VON BOCHMANN (**),
R. C. A. BROWN, F. J. M. FARLEY (***), M. GIESCH, H. JÖSTLEIN (**),
S. VAN DER MEER, E. PICASSO and R. W. WILLIAMS (**)
CERN - Geneva

(ricevuto il 14 Maggio 1971)

Summary. — The anomalous magnetic moment $a \equiv \frac{1}{2}(g-2)$ of the muon has been measured in the CERN muon storage ring. The result is $(116\,616 \pm 31)\cdot 10^{-8}$ compared with the theoretical value $(116\,588 \pm 2)\cdot 10^{-8}$ showing agreement to (240 ± 270) parts per million. The lifetime of muons moving in a circular orbit with $\gamma = 12$ was found to agree with the time dilation predicted by special relativity to within 1.1%. Details are given of the storage ring magnet, the instrumentation and the data analysis. The theoretical implications of the result are discussed.

1. - Introduction.

In a series of experiments carried out at CERN in the period 1958-1961, the anomalous part, $a \equiv \frac{1}{2}(g-2)$, of the g-factor of the muon was measured (1); it was found to agree with theory to within the estimated experi-

(*) Present address: Institute for High-Energy Physics of the Austrian Academy of Sciences, Vienna.
(**) Present address: Department of Physics, McGill University, Montreal, Quebec.
(***) Present address: Royal Military College of Science, Shrivenham, Wiltshire.
(**) Present address: Department of Physics, University of Rochester, Rochester, N.Y.
(**) Present address: Department of Physics, University of Washington, Seattle, Wash.
(1) G. CHARPAK, F. J. M. FARLEY, R. L. GARWIN, T. MULLER, J. C. SENS, V. L. TELEGDI and A. ZICHICHI: *Phys. Rev. Lett.*, **6**, 128 (1961); G. CHARPAK, F. J. M. FARLEY, R. L. GARWIN, T. MULLER, J. C. SENS and A. ZICHICHI: *Phys. Lett.*, **1**, 16 (1962); *Nuovo Cimento*, **37**, 1241 (1961). See also G. R. HENRY, G. SCHRANK and R. A. SWANSON: *Nuovo Cimento*, **63** A, 995 (1969).

mental error of $\pm 0.4\,\%$. This established what had previously been suspected, that the properties of the muon correspond exactly to those of a heavy electron. Apart from their masses and their association in weak interactions with two distinct kinds of neutrino, the two particles appeared to be identical. This experiment also tested indirectly the theory of quantum electrodynamics (QED) up to $q^2 \sim (1\ \mathrm{GeV})^2$, and was at the time the best test of the theory at short distances.

It was clearly important to pursue this measurement to higher levels of accuracy. To understand the μ-e problem we must search for further differences between the two particles. The magnetic moment, which carries information about the muon coupling to other fields, and the spatial structure of the muon electromagnetic vertex (if any), is a very sensitive diagnostic. A difference in the theoretical value, if established at a higher level of accuracy, would be an important experimental datum.

If, on the other hand, a more accurate measurement turned out to agree with theory, it would establish the validity of QED at higher q^2. A number of recent experiments [2] (lepton pair production, wide-angle bremsstrahlung, electron-electron and electron-positron colliding beam, e-p and μ-p scattering) have explored QED at $q^2 \sim ((1 \div 5)\ \mathrm{GeV})^2$, but the muon $(g-2)$ experiment is still the only measurement on the muon which involves electrodynamics only and is not contaminated by the presence of strongly interacting particles as part of the experiment.

Preliminary reports of our new series of measurements using the CERN muon storage ring have already been published [3-5]. As before, the measurement is accomplished by injecting polarized muons into an almost uniform

---

[2] For recent reviews, see F. J. M. FARLEY: *Riv. Nuovo Cimento*, **1**, 59 (1969); S. J. BRODSKY: *Proceedings of the International Symposium on Electron and Photon Interactions* (Daresbury, 1969); S. J. BRODSKY and S. D. DRELL: *Ann. Rev. Nucl. Sci.* (in press); E. PICASSO: in *High-Energy Physics and Nuclear Structure*, edited by S. DEVONS (New York, 1970), p. 615; R. WILSON: *XV International Conference on High-Energy Physics* (Kiev, 1970).

[3] F. J. M. FARLEY, J. BAILEY, R. C. A. BROWN, M. GIESCH, H. JÖSTLEIN, S. VAN DER MEER, E. PICASSO and M. TANNENBAUM: *Nuovo Cimento*, **45** A, 281 (1966).

[4] F. J. M. FARLEY, J. BAILEY, R. C. A. BROWN, M. GIESCH, H. JÖSTLEIN, S. VAN DER MEER and E. PICASSO: *The CERN Muon Storage Ring, Electron-Positron Colliding Beam Symposium*, Chap. VIII (Orsay-Saclay, 1966), p. 1; J. BAILEY, W. BARTL, R. C. A. BROWN, F. J. M. FARLEY, H. JÖSTLEIN, S. VAN DER MEER and E. PICASSO: *The anomalous magnetic moment of the* μ^-, in *Proceedings of the International Symposium on Electron and Photon Interactions at High Energy* (Stanford, Cal., 1967), p. 48; J. BAILEY, W. BARTL, G. VON BOCHMANN, R. C. A. BROWN, F. J. M. FARLEY, H. JÖSTLEIN, E. PICASSO and R. W. WILLIAMS: *Precision measurement of the anomalous magnetic moment of the muon*, paper No. 405 submitted to the *XV International Conference on High-Energy Physics, Vienna, 1968* (Geneva, 1968).

[5] J. BAILEY, W. BARTL, G. VON BOCHMANN, R. C. A. BROWN, F. J. M. FARLEY, H. JÖSTLEIN, E. PICASSO and R. W. WILLIAMS: *Phys. Lett.*, **28** B, 287 (1968).

magnetic field B ($\sim$17 kG). The anomalous moment causes the spin to turn faster than the momentum vector, the relative angular velocity in the laboratory frame being

$$\omega_a = a(e/m_0 c)\bar{B}\,, \tag{1}$$

where $\bar{B}$ is the time-average magnetic field for the ensemble of muons that contribute to the data. The time scale of previous experiments was limited to a few microseconds by the natural decay of the muon population ($\tau_0 \sim 2.2$ μs), and therefore only two anomalous precession cycles (of ~ 4 μs period) could be recorded. Coupled with the finite accuracy to which the spin direction can be observed, this was a major factor in the experimental error.

In the new experiment, the muons are highly relativistic ($\gamma \equiv (1-\beta^2)^{-\frac{1}{2}} \sim 12$), and the lifetime is increased by Einstein time dilation to $\tau = \gamma\tau_0 \sim 27$ μs. As there is no power of γ in eq. (1), the anomalous precession continues at the same rate, and we can record many (~ 50) precession cycles.

The muon momentum is now 1.27 GeV/c, implying an orbit diameter of 5 m. To carry out the measurement with reasonable economy, it is necessary to devise entirely new methods of injecting and storing polarized muons in a magnetic field, and of recording the spin-momentum angle as a function of time. We use a weak-focusing ring magnet, continuous in azimuth, with aperture 5.5 cm × 16 cm and $n = 0.13$. The cross-section is C-shaped with the yoke on the outside (see Figs. 1 and 2).

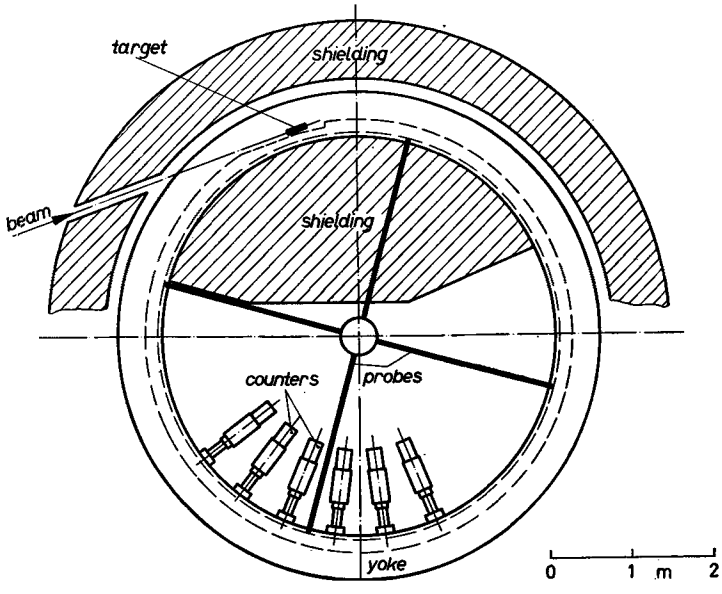

Fig. 1. – Plan of 5 m diameter ring magnet. The proton beam enters through a hole in the yoke and hits a target in the magnetic field. Muons created by π-μ decay are stored. The counters detect electrons from μ-e decay. The four probes of the NMR magnetometers are injected into specific locations on the muon orbit every 100 PS cycles.

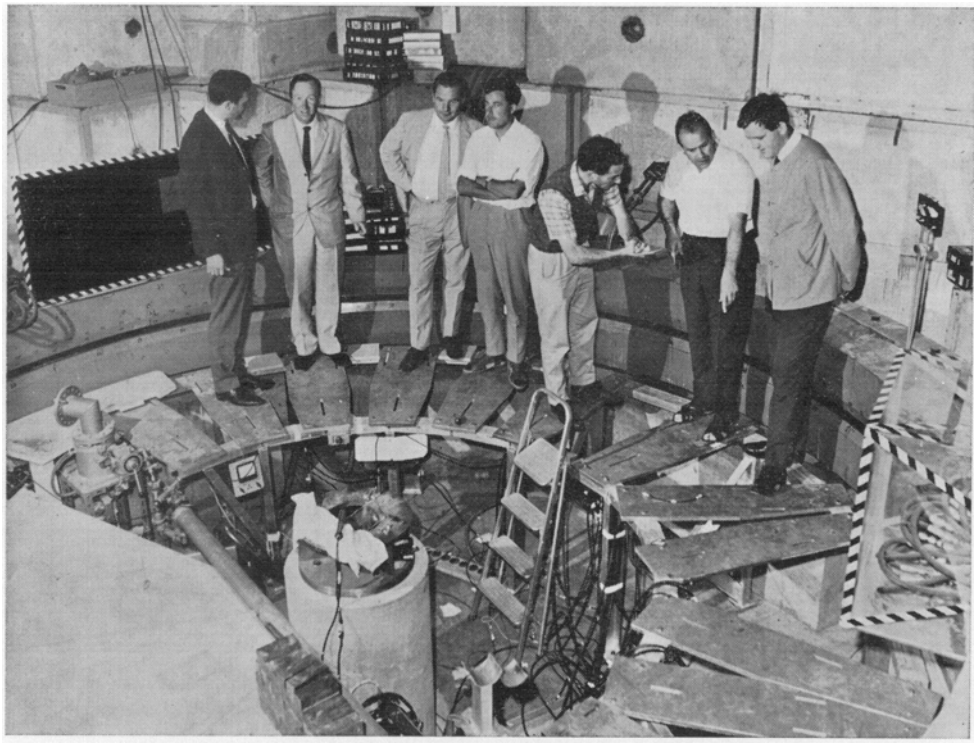

Fig. 2. – General view of the muon storage ring. The shielding inside the ring itself protects the counters from the initial blast of radiation. The pillar in the centre provides a fixed pivot for magnetic field surveys. It also supports four probes, which carry automatic NMR proton resonance magnetometers for monitoring the magnetic field. (*l. to r., van der Meer, Farley, Giesch, Brown, Bailey, Picasso, Jöstlein*).

The injection of muons is accomplished as follows. A beam of 10 GeV protons is ejected from the CERN Proton Synchrotron (PS) and focused onto a target inside the storage ring. Here $\sim 70\,\%$ of the protons interact, creating π^- of ~ 1.3 GeV/c which start to turn in the ring. The pion lifetime is such that in one turn 20 % of the π^- decay. The exactly forward decay creates μ^- of 0.1 % higher momentum, and these muons, together with undecayed π^- and stable particles from the target, will eventually hit the target assembly and be lost. However, decay of π^- at small forward angles gives rise to μ^- of slightly lower momentum, and some of these fall onto orbits which miss the target assembly and remain permanently stored in the ring. Thus the perturbation, essential for inflection into any circular machine, is here achieved by the shrinking of the orbit arising from the change of momentum in π-μ decays and/or by the change in angle at the decay point which may result in a μ^- with smaller oscillation amplitude than its parent π^-. The muons injected by this process are forward polarized on average. A pulsed magnetic

horn was used around the target during part of the experiment to increase the forward π^- flux.

The muon precession can be recorded by observing the decay in flight of muons in the ring magnet. If the decay electron is emitted forwards, with top energy in the centre-of-mass β-spectrum, it will have 0.2 % more laboratory momentum than the muon and will remain stored in the ring. Other decay electrons have less momentum and tend to spiral towards the inside of the ring. About 50 % of these electrons hit the magnet poles and are lost. The rest emerge with equal probability all around the ring and some of them hit the detectors.

Our detectors respond to decay electrons of energy greater than a minimum value $E_{\min}$ (say 750 MeV). To have this high an energy in the laboratory, the electron must *a*) be near the top end of the β-spectrum in the muon rest frame (high asymmetry parameter ([6])) and *b*) it must be emitted more or less forwards in the muon rest frame. Electrons emitted at smaller forward angles have higher energies in the laboratory, and so a counter with high energy threshold in the laboratory is equivalent, in the muon rest frame, to a telescope observing a small angular interval around the direction of motion. Therefore, as the muon spin rotates relative to its momentum vector according to eq. (1), the observed counting rate is modulated according to

$$N(t) = N_0 \exp[-t/\tau]\{1 - A\cos(\omega_a t + \varphi)\}, \tag{2}$$

and the frequency ω_a can be read from the data.

The magnetic field $\bar{B}$ is measured in terms of the corresponding mean proton precession frequency $\bar{\omega}_p$ for protons in water. The value of (e/m_0c) for the muon is obtained from the ratio of muon to proton precession frequencies at rest in the same field, $\lambda \equiv \omega_\mu/\omega_p$, which has been accurately measured for muons stopped in water and other substances relative to protons in water. We have

$$(e/m_0c)\bar{B} = \lambda(1+\varepsilon)(1+a)^{-1}\bar{\omega}_p, \tag{3}$$

where the correction factor $(1+\varepsilon)$ is the ratio of the field in vacuum to the diamagnetically shielded field of the muon in water ([7,8]). In effect, the proton NMR magnetometer is used as a link to connect two independent experiments on muon precession.

([6]) C. BOUCHIAT and L. MICHEL: *Phys. Rev.*, **106**, 170 (1957).

([7]) J. F. HAGUE, J. E. ROTHBERG, A. SCHENCK, D. L. WILLIAMS, R. W. WILLIAMS, K. K. YOUNG and K. M. CROWE: *Phys. Rev. Lett.*, **25**, 628 (1970); D. P. HUTCHINSON, F. L. LARSEN, N. C. SCHOEN, D. I. SOBER and A. S. KANOFSKY: *Phys. Rev. Lett.*, **24**, 1254 (1970).

([8]) M. A. RUDERMAN: *Phys. Rev. Lett.*, **17**, 794 (1968).

Equations (1) and (3) yield for the ratio $(\omega_a/\bar{\omega}_p)$ which we measure

$$\omega_a/\bar{\omega}_p = a(1+a)^{-1}\lambda(1+\varepsilon)\,. \tag{4}$$

As the radial magnetic gradient necessary for vertical focusing implies a field variation of 0.4% over the 8 cm radial aperture of the muon storage region, a major problem is to determine the mean radius of the ensemble of muons which contribute to our counts. This has been obtained by measurements related to the rotation frequency ω_r of the muons. As the injection pulse is only $(5 \div 10)$ ns long, and the rotation period $T = 2\pi\varrho/\beta c$ is about 52.5 ns, the muons are initially bunched, and the counting rate in the decay-electron counters is modulated during the first few microseconds. Analysis of the modulated records yields the mean radius to ± 2 mm (see Sect. **6**).

The radius of the ring is chosen in such a way that if several RF bunches are ejected in succession from the PS (spacing 105 ns), the corresponding muon bunches are superposed in the ring. As a result, the mean radius can be found even when multibunch injection is used.

1'1. *The stored muon intensity.* – The method used for trapping muons is to inject protons into the ring and have them interact with a target located at the outer limit of the storage region. The pions, produced at about zero degrees and having a momentum $\sim 1\%$ larger than that of the stored muons at the centre of the aperture (p_0), travel round the ring for nearly four revolutions before they again hit the target. Most of them will decay before this, so that the fraction of stored muons produced per circulating pion is rather high (typically of the order of one per thousand). However, a considerable number of pions with momentum higher than p_0 and a higher value of the injection angle will also travel inside the ring long enough to produce a greater number of stored muons. As the $\pi\mu$ decay need no longer be in the forward direction, these reduce the average polarization of the muon beam.

In order to find the number of stored muons N_μ as well as the polarization, both longitudinal (P_l) and radial (P_r), as a function of the momenta and of the pion injection angle, we used a Monte Carlo calculation; this is described in Appendix A. The program also gives the number of muons produced per pion (trapping efficiency) as a function of the above quantities.

The proton energy of the primary beam is 10.5 GeV, and we assume a proton intensity of 10^{12} per PS burst. The assumed pion yield is 1.0 $(\mathrm{GeV/c \cdot sr})^{-1}$, and the target efficiency (probability of proton interaction times probability for pion to escape) is 0.4. The ring parameters are: i) semi-horizontal aperture, 3.9 cm; ii) semi-vertical aperture, 2.2 cm; iii) radius of the muon storage ring at the centre of the aperture, 250 cm; iv) field index, 0.13.

In Table I are given the results for the expected values, normalized to one RF bunch of the PS ($5 \cdot 10^{10}$ protons per RF bunch).

TABLE I. – *Theoretical predictions for* μ^- *runs.*

Total number of stored muons	118
Mean longitudinal polarization	0.263
Mean radial polarization (positive in wards)	0.044
Mean radius of the muon distribution (in cm)	249.61

The method of injection used is very simple, but has the following disadvantages:

i) low muon polarization due to muons from a wide range of pion momenta,

ii) high general background,

iii) contamination by electrons at early times,

iv) low average trapping efficiency.

To compensate for the low trapping efficiency, we are storing muons from a wide range of pion momenta. As a consequence, the mean initial value of the longitudinal polarization is only about 26 %.

In Fig. 3 the dependence of the longitudinal and radial polarizations as a function of radius is given. The number of muons produced per pion (trapping efficiency) as a function of the pion momentum is shown in Fig. 4. The trapping efficiency has a maximum value of $5 \cdot 10^{-3}$ at a pion momentum $\sim +1.01 p_0$, and drops to about $4 \cdot 10^{-4}$ at a pion momentum $\sim +1.5 p_0$. One

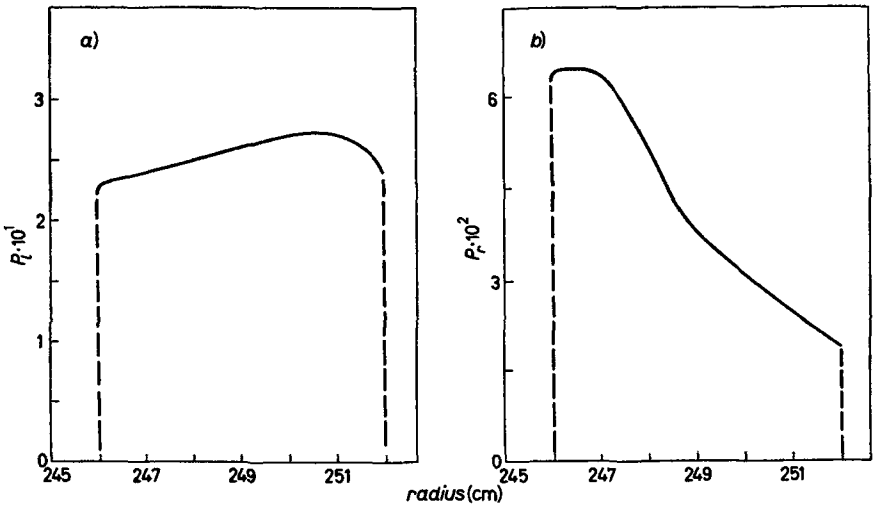

Fig. 3. – Longitudinal and radial polarization of the stored muons. The average values of the longitudinal and radial polarization are *a*) 0.26 and *b*) 0.044, respectively.

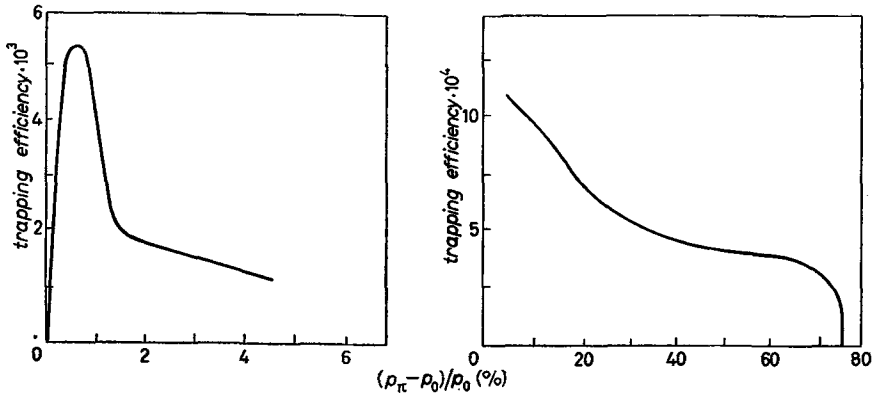

Fig. 4. – Number of muons produced per pion (*trapping efficiency*) as a function of the pion momentum. Approximately only one-fourth of the stored muons are produced by the circulating pions within a momentum of $(1.00 \div 1.03)\, p_0$, p_0 being the momentum of the stored muons at the centre of the muon storage ring aperture.

can deduce from Fig. 4 that approximately only one-fourth of the stored muons are produced by the circulating pions within a momentum of $(1.00 \div 1.03)p_0$.

The longitudinal polarization goes from a value of 0.996 (at $p_\pi = 1.007p_0$) to 0.860 (at $p_\pi = 1.034p_0$), and changes sign at about $p_\pi = +1.27p_0$; at $p_\pi = 1.5p_0$ its value is ~ -0.554. The weighted average is 0.26.

A high muon polarization was obtained during the run with the magnetic horn, showing that in this case the stored muons come predominantly from the decay of 1.3 GeV/c pions circulating in the ring (see Subsect. 5·2). Higher-energy pions are not well focused by the horn.

With the direction of the magnetic field reversed, the predicted number of positive muons stored in the ring has been evaluated to be ~ 160 per PS bunch. The mean values of the radial and longitudinal polarizations and the mean radius of the muon distribution are almost unchanged. The fraction of muons produced by the decay in flight of kaons was evaluated and found to be less than 1%: values of the longitudinal and radial components of the polarization were found to be comparable to those of the muons produced by pions.

1·2. *Asymmetry considerations and the optimization of* NA^2. – It can be shown from consideration of the data-fitting statistics that the error in ω_a is approximately

$$\sigma(\omega_a) \approx (\gamma\tau_0 \cdot A\sqrt{N_\mu \eta})^{-1}, \tag{5}$$

where τ_0 is the lifetime at rest, A is the asymmetry, N_μ is the number of stored muons, and η is the detection efficiency for the decay electrons. In order to

minimize the statistical error in the angular frequency ω_a, we must optimize $N_e A^2$, where $N_e \equiv N_\mu \eta$ is the number of recorded decay electrons. The experimental parameter is E_{min}, the threshold energy for detection of the electrons. Raising the value of E_{min} increases A at the expense of N_e.

To find the dependence of A and N_e on E_{min}, including the efficiency η which depends on the details of the escape of the electrons from the magnet, we used a Monte Carlo calculation described in Appendix B.

An analytical calculation (*) of the dependence of A and N_e on E_{min} proved possible, under the assumption that $\eta =$ constant, and with the aid of the standard V-A decay-electron distribution function and extreme-relativistic approximation. The result, in terms of x, the ratio of E_{min} to the maximum value of E, is

$$N_e = \frac{N_0}{3}(1-x)^2(3-x-x^2)\,, \tag{6}$$

$$A = P\frac{x(1+2x)}{3+x-x^2}\,. \tag{7}$$

Here P is the polarization of the sample of muons. The product $N_e A^2$ must be maximized to obtain the most efficient running conditions; this implies $x \approx 0.6$ or $E_{min} = 780$ MeV. Curves of N_e, A, and $N_e A^2$ are shown in Fig. 5.

It is possible that electrons produced at certain angles and energies in the laboratory frame may be lost. The field tends to bend the electrons inward towards the counters so that some electrons emitted outwards from the ring are

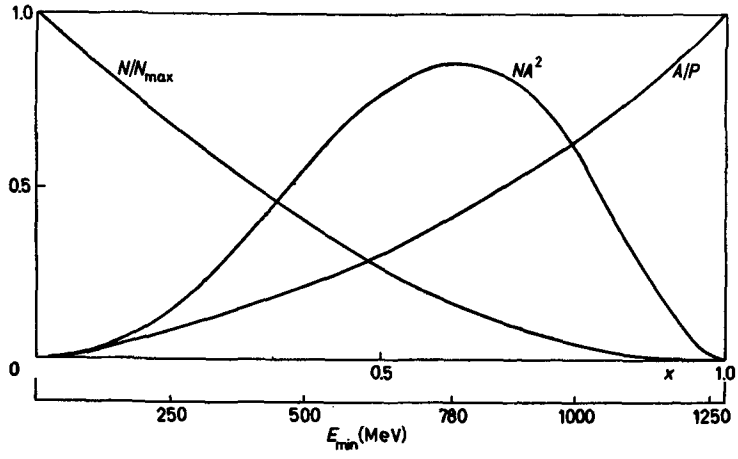

Fig. 5. – Dependence of the number of decay electrons N, the asymmetry coefficient A, and NA^2, *vs.* energy threshold E_{min}. The maximum value of NA^2 is obtained at $E_{min} = 780$ MeV.

(*) We are indebted to P. GODDARD for this treatment of the problem.

still detected, but others may be lost vertically. Detection in this case would depend not only on the electron energy in the laboratory frame but also on the polar angles θ, φ of the direction of emission of the electron relative to the muon direction. All these effects, including the dependence of the geometrical efficiency as a function of E_e and of the angle of emergence from the ring, were taken properly into account in the Monte Carlo calculation described in Appendix B. It is gratifying to find that the two methods agree well.

The above calculations were essential for designing the detection system but are not needed for computing, in first order, any correction to ω_a and ω_r.

The conclusion of the calculation can be summarised by saying that if the detectors respond to decay electrons of energy greater than a minimum value $E_{\min} \sim 780$ MeV, they are equivalent, in the muon rest frame, to a telescope observing a small angular interval around the direction of motion. If a higher threshold energy $E_{\min}$ is selected, one expects a smaller number of decay electrons, but the effective asymmetry parameter A will be higher, tending to 1 as $E_{\min}$ approaches the maximum. As $E_{\min}$ is reduced, the number of electrons rises but the asymmetry drops. The above-mentioned value of ~ 780 MeV is expected to be optimum (maximum value of NA^2) for the determination of ω_a. From the Monte Carlo calculation we find that the fraction of decay electrons with energy greater than 780 MeV, hitting detectors placed all around the ring, is about 8 % of the number of stored muons. For an energy cut of ~ 780 MeV we would have $A/P = 0.42$. From the injection program we predict an average forward polarization of the circulating negative muons of about 26 %; therefore the predicted value of the asymmetry parameter A (eq. (2)) will be around 11 %. The above results are obtained under the assumption that the electron detectors have a perfect energy resolution. The predicted number of decay electrons per counter per $3.5 \cdot 10^{10}$ injected protons (1 RF bunch of PS) is ~ 0.4 for a counter threshold of 780 MeV.

2. – The ring magnet.

The storage ring is a continuous, circular, C-sectional magnet without straight sections, with the aperture facing the centre of the ring (see Fig. 1 and 2). The diameter of the orbit at the centre of the aperture is 5 m. The aperture between the magnet pole faces is 55 mm high by 160 mm wide: but owing to the presence of an aluminium vacuum chamber, target and field measuring probes, the aperture available for particle storage is only 44×78 mm. The magnet is of the weak focusing type, with a field index

$$n = -\frac{\varrho}{B}\frac{\mathrm{d}B}{\mathrm{d}\varrho} = +0.13 \tag{8}$$

at a normal working field of 17.2 kG.

The coils are enclosed within the yoke of the magnet, and are split into two « pancakes » which are positioned symmetrically above and below the centre of the aperture. By suppressing the conventional coils on the outside of the pole pieces, improved access is obtained for large detectors to be brought close to the magnet aperture: some economic savings are also realized. However, this arrangement results in a leakage field spreading beyond the magnet aperture, amounting to 1 kG in the region of the counters and 0.5 kG at the centre of the ring. Current and cooling-water connections to the coils are made at two points, 180° apart, through openings in the magnet yoke. The presence of these openings results in a drop in the field at these points amounting to 1.5%, while field variations of $\sim 0.5\%$ occur at the junctions of the eight segments into which the magnet is azimuthally divided (see Fig. 6). The normal working current is 2460 A at about 600 V, supplied by a 1.3 MW generator.

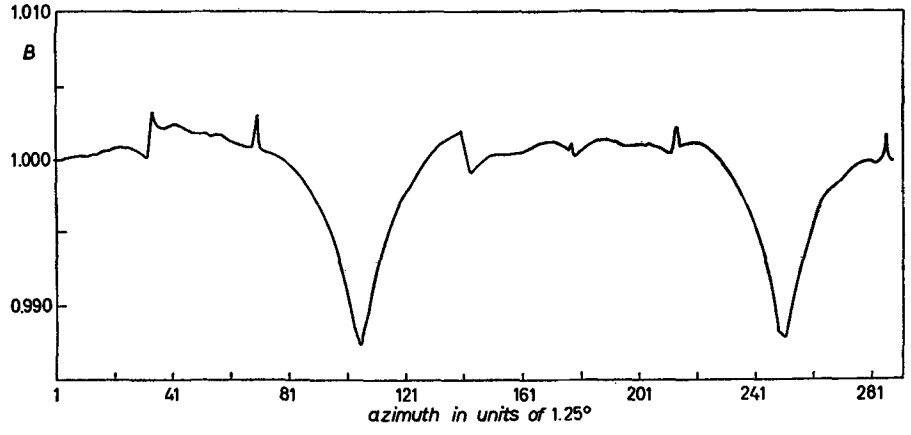

Fig. 6. – Azimuthal field distribution. Current and cooling-water connections to the coils are made at two points, 180° apart, through openings in the magnet yoke. The presence of these openings results in a drop in the field at these points of about 1.5%.

During the data-collecting runs the absolute magnetic field is measured by proton resonance at four monitor positions (see Fig. 1). The NMR probes are pneumatically driven to the centre of the aperture, approximately every 4 min. The field shape all over the muon storage region is established by mapping with proton resonance probes both before and after the run. All radial positions are established with reference to a pillar at the centre of the ring, independent of thermal expansion of the magnet. Special precautions ensure the long-term reproducibility of the average field, which is ~ 13 ppm (parts per million) relative to the four monitor positions.

2·1. *Proton-resonance magnetometer.* – To measure magnetic fields to an absolute precision better than 10 ppm, we developed a proton resonance mag-

netometer, whose frequency is « locked » to the magnetic field by a servo system.

A block diagram of the instrument ([9,10]) is shown in Fig. 7. The probe is of the absorption type ([1]), with a sample of 0.1 molar $NiSO_4$ contained in a cylindrical tube of 1.6 mm bore. The probe is driven by 1 V r.m.s. at about

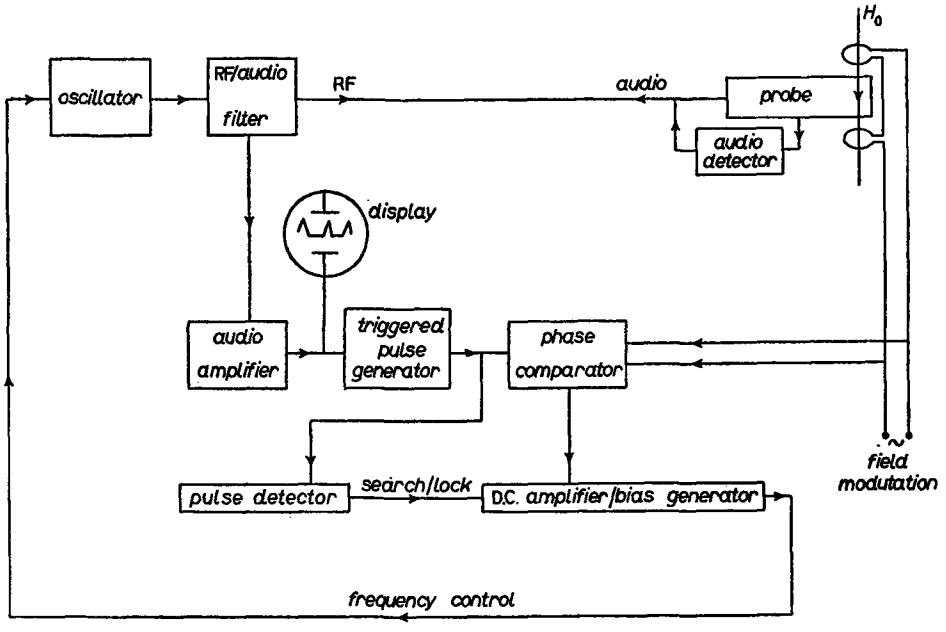

Fig. 7. – Block diagram of the proton-resonance magnetometer, whose frequency is « locked » to the magnetic field by a servo system.

72 MHz; the resonance signal is detected locally and returned to the main unit as a low-frequency pulse along the coaxial line from the driving oscillator. This technique permits the probe to be used up to 20 m from the main unit. The phase of the resonance signal is compared with that of the small modulating field (± 5 G at 50 Hz), thus generating an error signal which is fed back to bring the frequency of the main oscillator onto the proton resonance frequency.

The alignment of the frequency with the field is monitored by a linear display ([9]) of the resonance signal on a cathode-ray tube (Fig. 8), which permits the servo system to be set up accurately. In the absence of resonance signals the instrument automatically searches a preset range until the resonance is

([9]) R. ARMSTRONG-BROWN: *Nucl. Instr. Meth.*, **60**, 265 (1968).
([10]) R. ARMSTRONG-BROWN: *Proton Resonance Calibration and Field Studies of the CERN Muon Storage Ring* (Geneva, 1969), CERN 69-8.

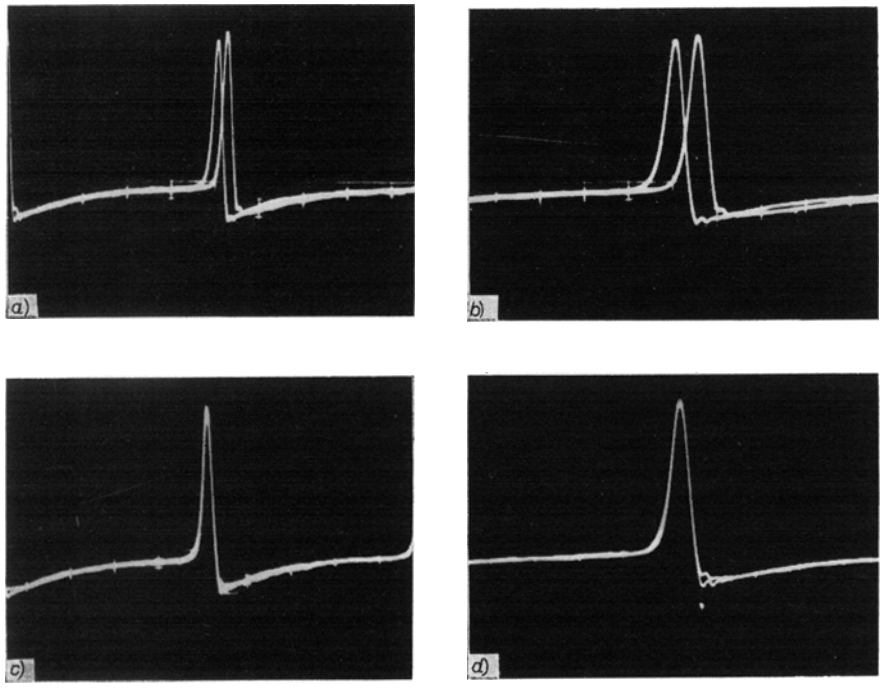

Fig. 8. – *a*) Typical display at 17 kG in a gradient of 10 G/cm, which causes line broadening. Misalignment 0.35 G. In an homogeneous field, an identical display would represent only 0.1 G misalignment. *b*) Same condition, display expanded $\times 2$. *c*) and *d*) are normal and expanded $\times 2$ displays, respectively, showing the sharpness of alignment that is attainable.

found and the lock re-established; during this period an interlock is set to prevent the recording of invalid frequency readings.

Corrections must be made to the field measured by the resonating protons in the sample to obtain the field for protons in pure water. These corrections have the form

$$B_p = B_0(1-\sigma)\,, \tag{9}$$

where σ is a screening factor. In our case the following corrections are considered ([10]): bulk diamagnetism of the sample $\sigma_d = 1.5$ ppm, bulk paramagnetism of the sample $\sigma_p = -(1.3 \pm 1.0)$ ppm, screening effects due to the probe materials $\sigma(\text{frame}) = (1.5 \pm 1.0)$ ppm, field reduction due to invar radius arms $\sigma = 3$ ppm, average effect of brass shielding $\sigma = -3$ ppm, giving $\sigma(\text{total}) = 1.7$ ppm (negligible). These corrections were relevant in calculating the absolute field in vacuum, but were, of course, not necessary in mapping the field shape.

Each magnetic measurement in a field of 17.2 kG, with the instruments properly aligned, is subject to a statistical error of ± 2 ppm due to residual jitter in the field-following system; plus a systematic error not exceeding 2 ppm when the corrections listed above are applied.

With the 1.6 mm diameter sample, the magnetometer is capable of working satisfactorily in the 10 G/cm focusing field gradient of the storage ring. However, if this gradient is cancelled at the sample with an opposing gradient, produced by compensating coils in the probe, the resonance signal is enhanced. Thus, by optimizing the resonance signal and measuring the current flowing in the compensating coils, it is possible to make point measurements of the gradients present in the field. These gradients are, in order of importance: i) radial $\mathrm{d}B_z/\mathrm{d}x$, the normal focusing quadrupole field; ii) skew $\mathrm{d}B_z/\mathrm{d}z$, a perturbing quadrupole field, whose axes are rotated by 45° relative to the radial component; and iii) azimuthal $\mathrm{d}B_z/\mathrm{d}\theta$. The method described is used in practice only for measuring the skew gradients in the field, and has a precision of $\pm 5\,\%$.

2·2. *The stabilizer.* – In order to improve the precision of magnetic measurements and to maintain a high degree of reproducibility in the magnetic field, it was found necessary to maintain the field level stable to about 10 ppm over long periods, and to raise and lower the magnet current in a reproducible manner. The magnet stabilizer ([10]) shown in Fig. 9 employs two independent field-measuring systems. Fast field changes are detected by a pick-up coil and integrator; slow or steady field changes are detected by comparison of the frequency of an independent servo magnetometer with that of a crystal oscillator. Error signals from both sources are added, amplified and fed back to a « variable resistor » in series with the main magnet windings. This has the effect of changing the voltage applied to the magnet, thus changing the field level in the sense required to reduce the error signal. The « variable resistor » is composed of a fixed resistance (20 mΩ, 2500 A) shunted by the active element, a transitor shunt which can be set to pass any current in the range $(0 \div 200)$ A.

When raising the magnet current, the voltage is raised at constant speed until the magnetometer locks at about 17 kG; under the opposing influences of the pick-up coil and the magnetometer error signals, the field is then raised asymptotically to the working value of 17.2 kG. The whole cycle takes about 90 s. It is standard procedure to cycle the field from zero to the working level and back to zero twice, and to take measurements only after raising the field to the working level for the third time.

The field stability is ± 2 ppm over periods of a few seconds, and remains within a total excursion of ± 20 ppm over periods of several weeks continuous running without realignment.

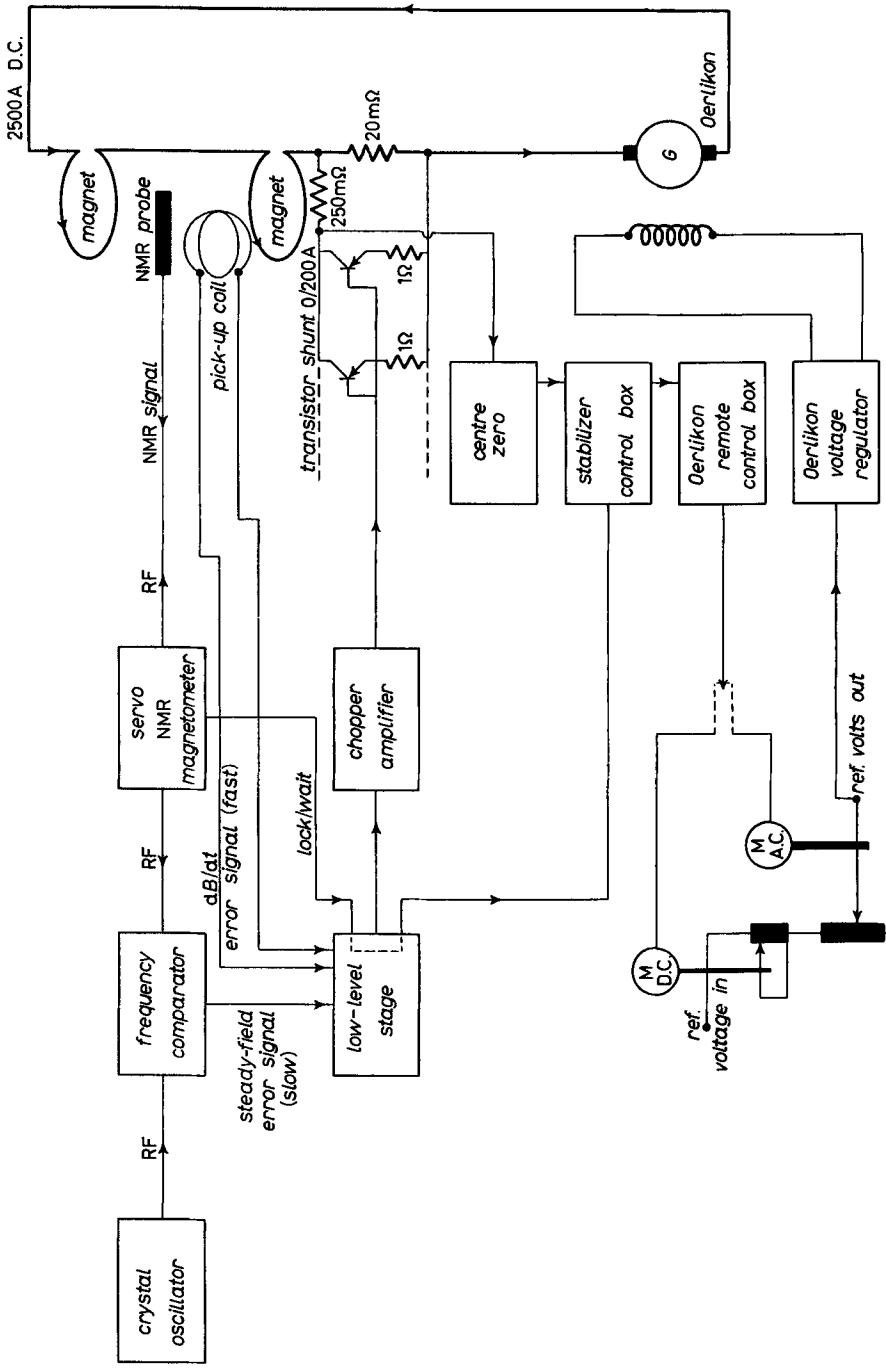

Fig. 9. – Block diagram of the field stabilizer, which employs two independent field-measuring systems. Fast field changes are detected by a pick-up coil and integrator; slow or steady field changes are detected by comparing the frequency of an independent servo magnetometer with that of a crystal oscillator.

2·3. *Magnetic field mapping.* – The field is carefully mapped, before and after periods of experimental running, at 1 cm intervals across the magnet aperture and at azimuthal intervals of 1.25°. For these measurements it is necessary to remove the vacuum chamber and some of the radiation shielding. All other features of the magnetic environment, such as the photomultiplier shields, iron-reinforced concrete shielding, etc., are left in their experimental positions. (The presence of a photomultiplier shield at a distance of 50 cm from the magnet reduces the field in the main gap by as much as 300 ppm.) The vacuum chamber and the dismounted concrete shielding have effects on the field of less than 2 ppm; a small correction is made for brass shielding used close to the magnet in the region of the target, which has the local effect of lowering the field by 12 ppm when it is replaced after the mapping is completed.

Two magnetometers are used during field mapping. One probe remains at a fixed position and measures a reference field level, while the mapping probe is supported on an invar radius arm from a pillar at the centre of the ring. This probe is moved successively to all the 2592 points to be mapped, the difference between the mapping and reference probe frequencies being measured at each point and automatically recorded by a scalar and teleprinter system ([10]). The measurements are processed by computer in order to check for inconsistencies, and the mean *relative field* (relative to the reference field) along a circular orbit is tabulated for each radius measured (see Table II).

During the measurement on the central orbit (radius 2500 mm) the relative field is carefully measured at the four points where the four monitor probes are to be located during the actual experimental running. This measurement

TABLE II. – *Magnetic field data for run* 9.

	Relative B averaged in azimuth		
Radius (cm)	Before run February 1967	After run June 1967	Average
246	1.001103	1.001042	1.001073
247	1.000649	1.000556	1.000603
248	1.000090	0.999996	1.000043
249	0.999521	0.999399	0.999460
250	0.998931	0.998891	0.998911
251	0.998436	0.998373	0.998405
252	0.997934	0.997875	0.997904
253	0.997483	0.997395	0.997444
254	0.997073	0.996992	0.997033
Mean of 4 monitor positions	1.000778	1.000760	1.000769
$\bar{B}(250)/\bar{B}_{\text{monitor}}$	0.998154	0.998132	0.998143

establishes the ratio of the mean relative field at radius 2500 to the mean relative field measured by the monitor probes. With the aid of this ratio, *absolute* measurements of the mean monitor frequency during the experiment permit the *absolute value* of the mean field at radius 2500 mm to be calculated: hence via the field map the absolute field at any other radius can also be established.

Both the mapping probe and the four monitor probes are supported on invar radius arms located on a concrete pillar at the centre of the ring. The length of these arms is calibrated against the CERN substandard metre to a precision of ± 0.02 mm. Field measurements are thus taken at fixed absolute radii, and no corrections are necessary for thermal expansion of the magnet. A possible correction for residual thermal expansion of the radius arms, 0.008 mm/°C, would result in a field correction of $3 \cdot 10^{-7}$/°C, which was not considered significant. However, small corrections have to be made for the magnetic influence of the invar arms on the probes (see above).

2·4. *Reproducibility.* – Extensive investigations were made of the reproducibility of the magnetic field ([10]). When the magnet is cycled and stabilized as described above, the typical relative field reproducibility for one point on consecutive cycles is about ± 25 ppm, and over a period of several months $\pm(30 \div 50)$ ppm. However, the mean relative field averaged around a circular orbit has a much better reproducibility.

The data for run 9 are given as an example in Table II. The change in mean field relative to the average of the four monitor positions was ± 11 ppm over a period of four months (*).

2·5. *Equilibrium orbit.* – In order to maximize the intensity of the stored particle beam, the equilibrium orbit must be as close as possible to a circle. As the field varied in azimuth by as much as 2%, it was necessary to calculate and adjust the shape of the equilibrium orbit.

The presence of an azimuthal variation $B_z' \cos k\theta$ of the vertical field B_z (at constant radius) will result in a radial perturbation of the equilibrium orbit of amplitude $\varrho_0 B_z'/B_z(k^2 + n - 1)$. We see that while the first order ($k = 1$) has a very large effect, higher-order field variations have a rapidly diminishing influence. In practice, a set of field measurements at radius 2500 mm is Fourier analysed for azimuthal variations up to the fourth order; their effect on the orbit is calculated via the above expression, and their contributions summed to arrive at the final equilibrium orbit. By making fine adjustments to the field level in the separate magnet sections, it is possible to optimize the lower-order Fourier coefficients of the field distribution, thus optimizing the equilibrium orbit in an iterative manner. This procedure

(*) As a result of improved methods ([10]), later runs had a reproducibility of ± 6 ppm.

is carried out before the complete field maps are measured. By this technique the radial variations of the equilibrium orbit may be reduced to ± 3 mm; the residual variations are due largely to the second-harmonic field variations introduced by the presence of the coil connections, which could not be completely compensated.

The vertical location of the equilibrium orbit lies at the mean vertical position of the median plane of the magnetic field. The median plane is defined to be the surface along which the radial component of the field B_ϱ is equal to zero. In order to measure this we place a search coil at the centre of the magnet aperture. The axis of rotation of this coil is aligned to the true vertical ± 0.005 mrad using a precision autocollimating theodolite ([10]), therefore the search coil links only with the B_ϱ-component of the field. We rotate the coil through 180° and integrate the output, adjusting the tilt of the magnet section and realigning the axis of the coil repeatedly until a null output is obtained. Thus the median plane is adjusted to pass through the centre of the coil. In this manner it is possible to align the mean position of the vertical closed orbit to within ± 1 mm of centre of the magnet aperture. Higher harmonics of the radial field cause perturbations which are attenuated with increasing order k as $n/(k^2-n)$. In general, only the first harmonic is significant, and has amplitude ± 1 mm.

3. – Electron detectors.

The counter used for detecting the electron from muon decay and for measuring its energy is a lead-scintillator sandwich. Alternating layers of lead (3 mm thick) and plastic scintillator (4 mm thick) are used, giving a total thickness of 20 radiation lengths. In principle, the whole energy of the incoming electron is absorbed, and the cascade shower is regularly sampled by the scintillators so, apart from fluctuations in the shower process, the size of the total pulse of light should be proportional to the electron energy.

The light is channelled by a polished aluminium light-pipe to 5″ photomultipliers (Philips type 58 AVP). In early experiments we used plastic light-pipes, but found that the background light originating in the plastic from general radiation near the ring was excessive. (Glass Čerenkov counters give better energy resolution, but the light output is small and is swamped by the signal from the plastic light-pipe; owing to total internal reflection, no signal is obtained if the Čerenkov glass is used with an air light-pipe.)

The counters were calibrated with a momentum-analysed electron beam, selected with the aid of a gas Čerenkov counter. Typical pulse-height spectra are shown in Fig. 10.

Individual pulse-height discriminators were set so that an electron of the chosen threshold energy would have a 50 % probability of giving a count. The

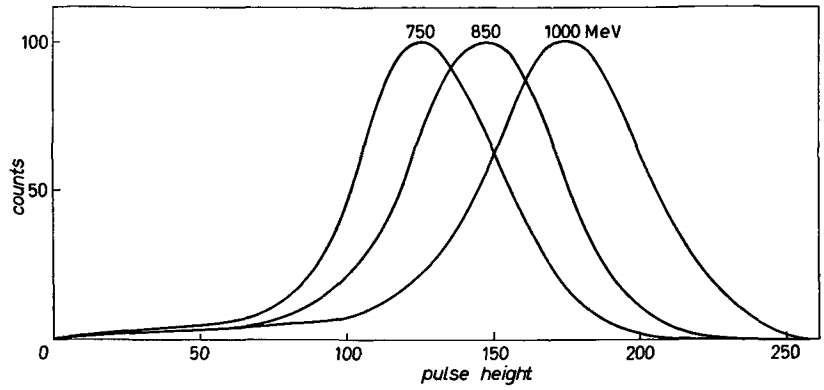

Fig. 10. – Typical pulse-height spectra of the counter used for detecting the decay electron and measuring its energy. The detector is a lead-scintillator sandwich of total thickness 20 radiation lengths.

outputs of all discriminators were usually combined together by a logical-OR circuit, and transmitted to the digitron for sorting into the appropriate time bins.

3·1. *Blanking system.* – It is necessary to switch off the detector electronics when the bunch of protons is injected into the ring. Secondary particles from the target making half a turn of the ring cause a large flash of light in the scintillators (called the «initial flash»), and this can paralyse the electronics for many microseconds. This is due partly to the heavy currents which flow in the final stages of the photomultiplier chain, causing reservoir capacities to be discharged, but more essentially to the discharging of the photocathode itself ([11,12]).

The surface resistance of the photocathode is several hundred kilohm per square. Together with its stray capacity, this makes a time constant of order 40 μs. Therefore, a large flash of light with its associated photocurrent can alter the photocathode potential, and upset the delicate electron collection optics at the input to the multiplier section. The response of the system then remains poor for many microseconds.

In our blanking system (Fig. 11) a large positive pulse (~300 V) is applied to the photocathode, causing all photoelectrons to return. This is achieved via a grid of thin wires 7 mm apart placed in front of the phototube. The capacity between the grid and the photocathode transmits the applied pulse. The same pulse must be applied to the photocathode connection itself, otherwise

([11]) F. J. M. FARLEY and B. S. CARTER: *Nucl. Instr. Meth.*, **28**, 279 (1964).
([12]) W. BARTL: *Gating of Photomultipliers* (Geneva, 1968), CERN 68-41.

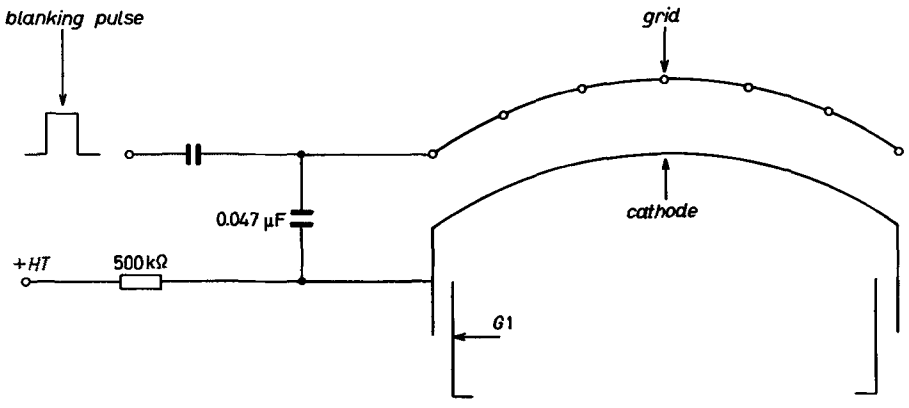

Fig. 11. – Block diagram of the blanking system. A large positive pulse (~ 300 V) is applied to the photocathode, causing all photoelectrons to return. This is achieved via a grid of thin wires, 7 mm apart, placed in front of the phototube.

current will flow, discharging the grid-to-photocathode capacity and leaving long-term changes in the cathode potential after the pulse has disappeared.

Simulating the initial flash with an intense light source we obtained the results shown in Fig. 12. The response is normal at 1 μs after the blanking is turned off, and it is not affected by the presence of the flash.

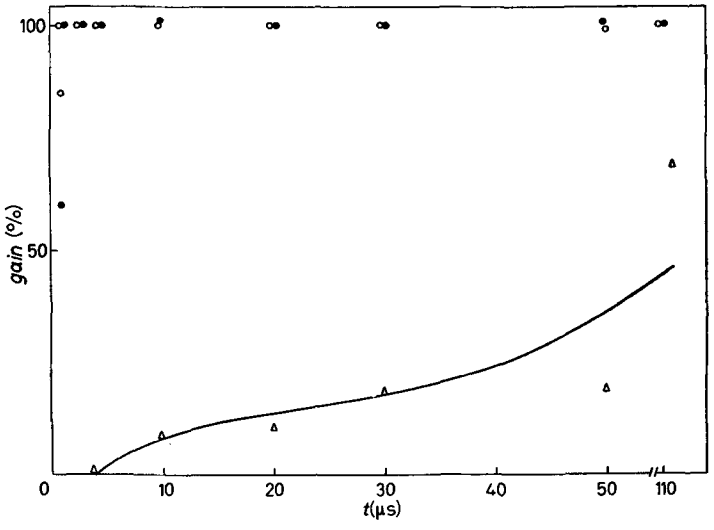

Fig. 12. – Gain of the 58 AVP photomultiplier as a function of time. The *initial flash* is simulated with an intense light source. The response is normal at 1 μs after the blanking is turned off, and it is not affected by the presence of the flash: o blanking; • blanking plus flash; ▵ flash only.

3·2. *Pick-up electrode.* – The start signal which initiates the electronic timing sequence needs to be reproducible from pulse to pulse, but its absolute point in time need not be known. An electrostatic pick-up pulse is obtained from the ejected proton beam a few metres upstream of the storage ring by means of a Faraday tube 1 m long. As well as triggering the digitron (see Sect. **5**), the area of the signal is digitized by a fast-pulse encoder so that a number proportional to the number of protons can be recorded on a scaler.

4. – Digitron.

4·1. *Outline.* – The function of the digitron ([13]) is to record the time of arrival t of each decay electron with respect to a *start* signal generated by the incoming proton beam. An absolute scale of time must be established so that frequencies read from the data are known in s^{-1}.

Following established practice, this is achieved by counting a known clock frequency ($f_{clock} = 200.020$ MHz), derived from a crystal-controlled oscillator, during the interval to be determined. The time scale is recorded digitally in increments of 5 ns. The scaler is started by the start signal derived from the proton beam and stopped by a signal from the decay electron. In our case, several decay electrons must be recorded for every cycle of the proton synchrotron: that is, each start signal may be followed by several *stop* signals, every one of which must be measured. This is achieved by using a large number of scalers, which all start to count the clock simultaneously when the start signal is received. It is arranged that the first stop signal stops the first scaler, the second stop signal stops the second scaler, and so on until all stops have been recorded. Any remaining scalers continue running until at $t \sim 300$ μs the train of clock pulses is turned off. The readings of all these remaining scalers should be the same, the so-called *final-stop* number, which provides a check on the correct operation of the scalers.

During the 2 s quiescent period between PS pulses, the scaler readings are transferred in succession to a data transfer unit (DTU), which writes the information onto magnetic tape. Simultaneously, the data can be transferred to a PDP-8 on-line computer, and to a modified TMC pulse-height analyser. These instruments are used to check the data, and to display histograms of counts *vs.* t which enable the progress of the experiment to be controlled. The final analysis of the data is made with a large computer from the complete information available on magnetic tape (see Sect. **6**). A block diagram is shown in Fig. 13.

([13]) Digitrons have been described by R. A. SWANSON: *Rev. Sci. Instr.*, **31**, 149 (1960); R. A. LUNDY: *Rev. Sci. Instr.*, **34**, 146 (1963); see also ref. ([1]).

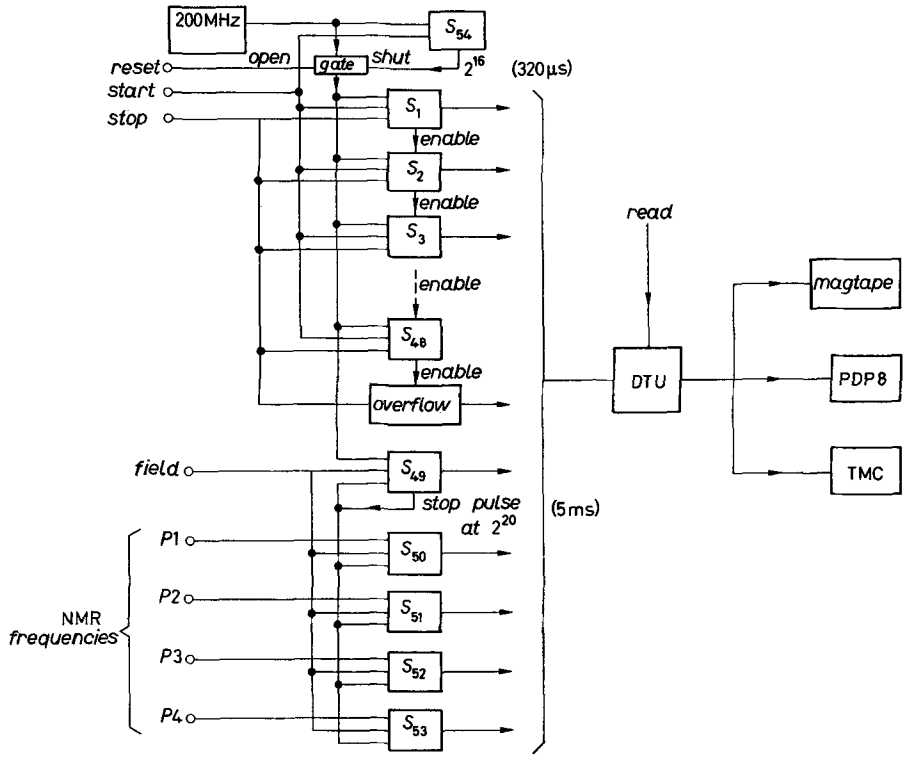

Fig. 13. – Block diagram of the digitron and data transfer unit (DTU) system. Several decay electrons must be recorded for every cycle of the proton synchrotron; that is, each start signal may be followed by several stop signals, each of which must be measured. This is achieved by using a large number of scalers, which all start to count the clock simultaneously when the start signal (derived from the proton beam) is received. The first stop signal (first decay electron) stops the first scaler, the second stop signal stops the second scaler, and so on until all stops have been recorded. During the 2 s quiescent period between PS pulses, the scaler readings are transferred in succession to a data transfer unit (DTU), which writes the information onto magnetic tape and simultaneously transfers it to a PDP-8 on-line computer and to a modified TMC pulse-height analyser: Pulse timings: reset — 50 ms, field (reset + 200 μs), start 0, stops (0 ÷ 300) μs, read + 10 ms. Reset connection to scalers not shown; reset puts all scalers into stopped state.

The crystal-controlled clock pulses are running continuously and are not synchronized with the start signal; therefore, for a fixed time interval, the result of a measurement is statistically distributed between two neighbouring 5 ns channels. From the counts C_n and $C_{(n+1)}$ in the two channels, the exact time t can be determined:

$$t = f_{\text{clock}}^{-1} \cdot \left[n + \frac{C_{(n+1)}}{C_n + C_{(n+1)}} \right] \tag{10}$$

subject to the usual statistical uncertainties. This formula is useful in testing with fixed pulse trains. When a continuous distribution in time is recorded, this computation is not relevant; the data are in effect folded with the triangular response function of each channel, which can be written

$$P_n(t) = \tfrac{1}{2}\{|y| + y\}\,, \tag{11}$$

where

$$y = 1 - |f_{\text{clock}} \cdot t - n|\,. \tag{12}$$

As $(ft - n)$ increases from -1 through 0 to $+1$, $P_n(t)$ rises linearly from 0 to 1, and then drops back again linearly to 0.

4·2. *Derandomizer.* – Some preprocessing of the start and stop signals is necessary before they are presented to the scalers, otherwise variations in the properties of the individual scalers may introduce timing errors. For example, if a clock pulse coincides with the start signal, it could be counted by some scalers but not by others, the result being dependent on small differences in the response of the scaler input circuits. The resulting difference of one channel could lead to unpredictable errors in the data. To avoid this, the raw start signal is first processed by a « derandomizer », the output of which is the clock pulse immediately following the input signal. This is then delayed by 2.5 ns

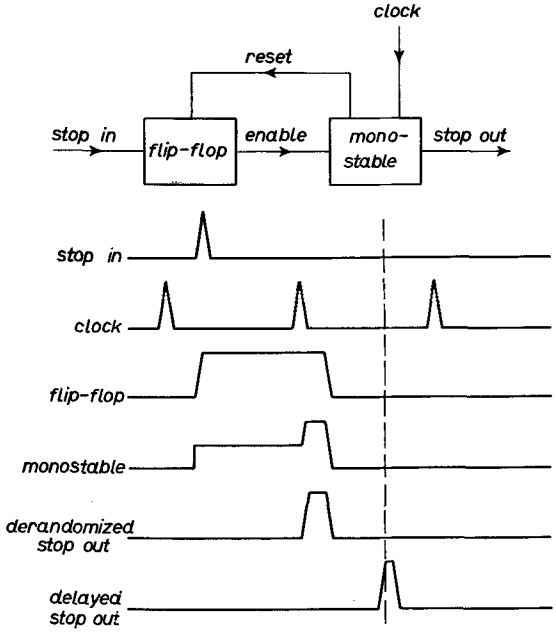

Fig. 14. – Block diagram of the derandomizer. The dead-time of the derandomizer is (5÷10) ns. The minimum spacing between the derandomizer output pulses is 10 ns. The output stop signal always comes halfway between clock pulses.

and arrives at the scaler just half-way between the clock pulses. Thus, the scaler is switched on about 2.5 ns before it is required to count. In this situation all scalers will have an identical response.

In a similar way the raw stop signals are derandomized by a second circuit, and the stop pulse fed to the scalers falls just half-way between the clock pulses. The time threshold between one channel and another is determined by the properties of the derandomizer. The decision is independent of the scaler, and is made in the same way for all stop signals, whether they arrive at early or late times. Thus, systematic timing errors which would give rise to errors in frequency ω_a are avoided. Such errors could arise, for example, because of the correlation between arrival time and the order number of a scaler: the first scaler always records the earliest arrival time.

A block diagram of the derandomizer is shown in Fig. 14. The dead-time of the derandomizer is $(5 \div 10)$ ns. The minimum spacing between the derandomized output pulses is 10 ns.

4·3. *Enable.* – The logic for stopping the scalers in turn on successive stop pulses is included in the input circuits of each scaler. For example, the stopping of scaler 1 generates a gate pulse called *enable* which allows the next stop signal to pass to scaler 2, and so on. The rise-time of these circuits is ~ 1 ns, so stop signals coming 5 ns apart could be recorded. (In fact, the minimum spacing is ~ 10 ns because of the derandomizer dead-time, see above.)

4·4. *Overflow.* – It occasionally happens that the number of stops to be recorded exceeds the number of scalers in the digitron. In this case an overflow indicator is set, and the read signal which initiates the transfer to the DTU is inhibited. The whole event is therefore discarded.

4·5. *Magnetic field measurement.* – As explained above, the magnetic field is measured during the run by NMR self-tuning magnetometers which can be driven pneumatically into the centre of the magnet aperture. The NMR frequencies (~ 70 MHz) are recorded by counting for a fixed time, which is itself obtained by scaling the 200 MHz clock. Thus the proton resonance frequency ω_p, as well as ω_a, are both measured relative to f_{clock}. As only the ratio ω_a/ω_p enters the calculation of a_{exp} (see eq. (4)), any error in f_{clock} cancels out. (Note, however, that the absolute value of f_{clock} is needed in computing the orbit radius from the rotation frequency ω_r, but to a considerably lower accuracy; see Sect. **6**.)

The method of measuring the NMR frequencies is indicated in Fig. 13. The NMR frequencies are counted for a 5 ms period defined by 2^{20} clock pulses. The process is initiated by a signal called *field* which occurs about 50 ms before the protons are ejected from the PS. The data are transferred by the

DTU to the magnetic tape and the on-line computer together with the digitron scaler readings.

Logical control is provided to ensure that the field is not measured unless the NMR probes are in their correct positions, and that the frequency-servo is working. Also the data are not written onto tape when there has been no start signal, and are held in the scalers without reset until the writing to magnetic tape is accomplished successfully.

4·6. *Splitting the digitron.* – The digitron, consisting of 48 scalers, may be subdivided in two distinct ways:

i) It can be split into two digitrons of 24 scalers each, both fed with the same stop signals. The first scaler of each set is *enabled* so that it will accept the first stop pulse; each digitron has its own overflow logic. In this case the two digitrons carry out the same task, and corresponding scalers should agree exactly. We ran the experiment this way for most of the data collection in order to guard against scaler errors.

ii) Alternatively, one may split the digitron into two or more subgroups of scalers, each fed with different stop pulses derived from independent counters or groups of counters. This is useful for studying the behaviour of individual counters either in setting up, or when some malfunction is suspected. A decision can be made later whether a particular subset of data is to be included in the analysis.

4·7. *Monitoring by* PDP-8. – In the early runs some malfunction of digitron scalers was detected, and data had to be rejected from the time of the last successful testing. In order to monitor the electronics continuously, we introduced the PDP-8 and split the digitron into two, as described in 4·6 i) above. All data were still written directly onto magnetic tape, but the PDP-8 made the following checks to confirm that:

i) corresponding scalers in the two digitrons agree,

ii) the scaler readings increase progressively,

iii) the *final stop* number is correct,

iv) the magnetic field scalers read within pre-set limits,

v) the incoming-proton beam is above a certain intensity.

If errors occurred, messages were generated so that appropriate corrective action could be initiated. (Note that in the final processing of the magnetic tape, any data showing errors i) to v) were rejected, see below.)

If the data were acceptable to the PDP-8, the figures were used to up-date the monitor histograms of counts *vs.* time. Two 1000-channel histograms were

constructed, one showing $(0 \div 5)\,\mu s$ in steps of 5 ns; the other showing $(0 \div 160)\,\mu s$ in steps of $0.16\,\mu s$ was obtained by ignoring the five least significant bits of the scaler readings.

In earlier runs, monitor histograms were obtained by transferring the scaler readings to a modified TMC 1024-channel pulse-height analyser. A special logic unit was constructed which added one count to an address derived from the scaler reading. Later this device was used in parallel with the PDP-8 to display selected subsets of the data, and could be used, for example, to check the performance of individual counters during the run.

4·8. *Routine tests.* – A number of regular routine tests were established to check the correct operation of the system.

i) The correct counting of all scalers and the read-out of all bits was checked by filling all scalers with the same number using a preset count unit, *e.g.* displaying all binary ones or all zeros. By writing on magnetic tape and calling for an octal dump from the main computer, it was established that all digits were correctly transferred throughout the system.

ii) Correct scaler operation at 200 MHz was checked by using stop signals at 25 MHz synchronized with the clock. Successive scaler readings should increase by 8, which is easily checked visually on the binary display.

iii) A train of 27 MHz crystal-controlled pulses, not synchronized with the clock, were used as stop signals. One of these pulses was selected by a gate and used as the start signal. The stops therefore always came at fixed times, equally spaced by 37 ns. If the equipment is cycled N times, each stop should give N counts, statistically divided between two adjacent channels, as illustrated in Table III. Any malfunctioning of a scaler would imply that the corresponding pair of channels would not add up to N; instead, counts would be spread over other channels. It was therefore easy to establish correct operation, or to identify any scaler that was giving errors.

4·9. *Special tests.* – To establish the overall accuracy of the digitron, the following tests were made. Using the 27 MHz crystal-controlled stop signals described in ii) above, the time t for each stop could be calculated using eq. (10); typical figures are given in Table III. To examine the consistency of the data, we plot $(t - 7.375\,m)$ *vs.* m, where m is the serial number of the stop signal. Figure 15 shows the result for the same set of data. The deviation of points from the best straight line is only 0.005 channel (0.025 ns), consistent with the expected statistical fluctuation and showing that the crystal pulses can be timed to this accuracy. From the slope of the line in Fig. 15 the crystal frequency is (27.1280 ± 0.0005) MHz, agreeing exactly with the determination by a frequency standard.

TABLE III. – *Digitron test data.*

Channel n	Counts C_n	Total for each pair	Mean time t (channels)	Serial number of stop m	$t - 7.375\,m$ (channels)
40	0				
1	0				
2	17944				
3	14824	32768	42.452	5	5.577
4	0				
5	0				
6	0				
7	0				
8	0				
9	5425				
50	27343	32768	49.834	6	5.584
1	0				
2	0				
3	0				
4	0				
5	0				
6	0				
7	25946				
8	6822	32768	57.208	7	5.583
9	0				
60	0				
1	0				
2	0				
3	0				
4	13692				
5	19076	32768	64.582	8	5.582
6	0				
7	0				
8	0				
9	0				
70	0				
1	1405				

TABLE III (*continued*).

Channel n	Counts C_n	Total for each pair	Mean time t (channels)	Serial number of stop m	$t-7.375m$ (channels)
2	31 363	32 768	71.957	9	5.582
3	0				
4	0				
5	0				
6	0				
7	0				
8	0				
9	21 912				
80	10 856	32 768	79.331	10	5.581

Data obtained with a train of 27.128 MHz crystal-controlled stop pulses. The time t for the m-th pulse is calculated from eq. (10) and compared with the linear relation $t = 7.375\,m$. Figure 15 is plotted from this Table. Note that the digitron was cycled 32 768 times, and therefore each stop pulse must be counted as often as this. The fact that each group adds to the correct total, and that the intermediate channels show zero counts, is a good test of the correct operation of the whole equipment.

In a similar test a gate was used, so that only one in five of the crystal pulses could reach the digitron, thus reducing the counting rate and giving a check on any rate-dependent shift in the time measurement. Such an effect could give an error in a_{exp} because the counting rate is high at early times and

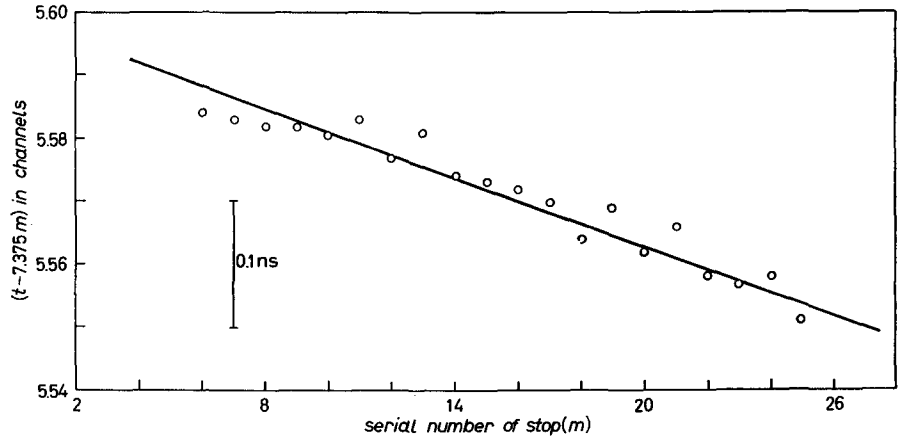

Fig. 15. – Plot of $(t-7.375\,m)$ in channels *vs.* the serial number of stop signal m. The deviation of points from the best straight line is 0.025 ns. From the slope of the line, the crystal frequency is (27.1280 ± 0.0005) MHz, in agreement with the determination by a frequency standard.

low at later ones. The test showed that for a stop rate of 27 MHz the shift is less than 0.1 ns, which is completely negligible for the experiment.

Tests were also made with random stop signals derived from a scintillation counter and radioactive source. To avoid correlated after-pulses from the photomultiplier, care must be taken to work at fairly low gain; but a high counting rate is needed to ensure that many stops occur in 300 μs and therefore many scalers of the digitron are active. As any event which overflows the digitron is not transferred by the DTU, there should be no slope in the data due to the corresponding loss of counts at late times.

A test with $5 \cdot 10^6$ total counts (giving $5 \cdot 10^3$ counts in each of 1000 channels) and covering the range $(0 \div 320)$ μs gave a flat distribution within statistical error. The slope was less than $3.6 \cdot 10^{-5}$ $(\mu s)^{-1}$ to 68 % confidence, implying an error of less than 0.1 % in the dilated muon lifetime.

In another test the random counts were modulated at a known frequency (~ 390 kHz) to give a ± 9 % modulation of the counting rate. The fitted frequency obtained from $2.1 \cdot 10^7$ counts agreed satisfactorily (discrepancy = $= (150 \pm 100)$ ppm).

5. – Operation of the muon storage ring.

In all experiments the signals from the counters were sorted in time by the digitron. We examined the record for a component with the correct exponential decay (27 μs), and a modulation of the counting rate at the expected $(g-2)$ precession frequency. This signature was used to identify stored muons. A number of secondary effects were observed, and a series of exploratory experiments were necessary to arrive at the final optimum configuration. These will now be briefly summarized.

5·1. *Electronic effects on counters, blanking.* – During the first turn many charged particles from the target emerge from the ring and can hit the counters; this is referred to as the *initial flash*. As a result, a large photocurrent flows and can discharge the potential applied to the photocathode. The effect is strongly reduced if the magnet is turned off. The *blanking* circuit described above (Fig. 11) reduces the problem, but we were only able to run satisfactorily with counters placed at about 180° in azimuth from the target, where the spill-out of particles is smallest. The effect was much worse when the magnetic horn was used round the target to increase the flux of circulating π; it was worse for μ^+ storage than for μ^- (presumably due to circulating protons). To obtain detailed data at very early times, it was necessary to reduce the intensity of the protons from the PS by putting an absorber in the beam (see Subsect. 6·2.2).

5·2. *Magnetic horn or simple target.* – The ring was operated with two types of target in which the protons interacted to produce pions:

i) A gold bar, 5 mm in diameter and 120 mm long, surrounded by a magnetic horn, pulsed to focus pions of the desired momentum. In this case, the horizontal aperture available for storing muons was 66.5 mm.

ii) A copper bar 4 mm in diameter and 16 cm long, leaving a larger aperture (78 mm wide) for muon storage. Alternatively, an aluminium target $6 \times 6 \times 500$ mm was used.

The decay electron counting rate is extrapolated to zero time to give an estimate of the number of stored muons. Figures are quoted for a single electron counter, using $3.5 \cdot 10^{10}$ injected protons (1 RF bunch of the PS). Running for μ^- with the magnetic horn, the counting rate was 0.4 per counter per pulse with a counter threshold of 1000 MeV, and the amplitude A of the $(g-2)$ modulation was 33 %. This corresponds to a high muon polarization, showing that the muons come predominantly from the decay of 1.3 GeV/c pions circulating in the ring. As expected, the horn enhances this flux, compared with the flux of higher-energy *unstored* pions.

However, owing to the reduced aperture, NA^2 was not significantly greater than for the simple target. On the other hand, the enhanced number of charged particles hitting the counters during the first turn greatly aggravated the problem of counter paralysis, and there was also some disturbance of the electronics by the large pulsed current flowing in the horn. We obtained a preliminary result [3] on μ^- using the horn, but preferred the simple target for collecting all the data reported in this paper.

Without the horn, with the target ii) above, the counting rate was 0.3 per counter per pulse at a decay electron threshold of 650 MeV for both μ^+ and μ^-, while the modulation amplitudes A were 12 % for μ^- and 8.5 % for μ^+. These rates and amplitudes agree rather well with those predicted in Sect. 1. The lower asymmetry parameter obtained with μ^+ is probably associated with the enhanced yield of high-energy π^+ (and K^+) from the primary target, but the difference is surprisingly large. Most of our data were taken with μ^- for this reason.

5·3. *Proton leakage from the* PS. – An efficient beam transport system links the muon storage ring to the PS. There is therefore a danger that protons scattered from the PS will enter the beam line, even when the pulsed ejection magnets are inactive, and so cause background counts in our counters. To guard against this danger, we installed in the beam line a pulsed sweeper magnet, which was turned on for 300 μs immediately after the ejected protons had passed. If this sweeper magnet was not used, we found an intense peak in the counting rate at 6 μs (three turns of the PS); see Fig. 16. This is related

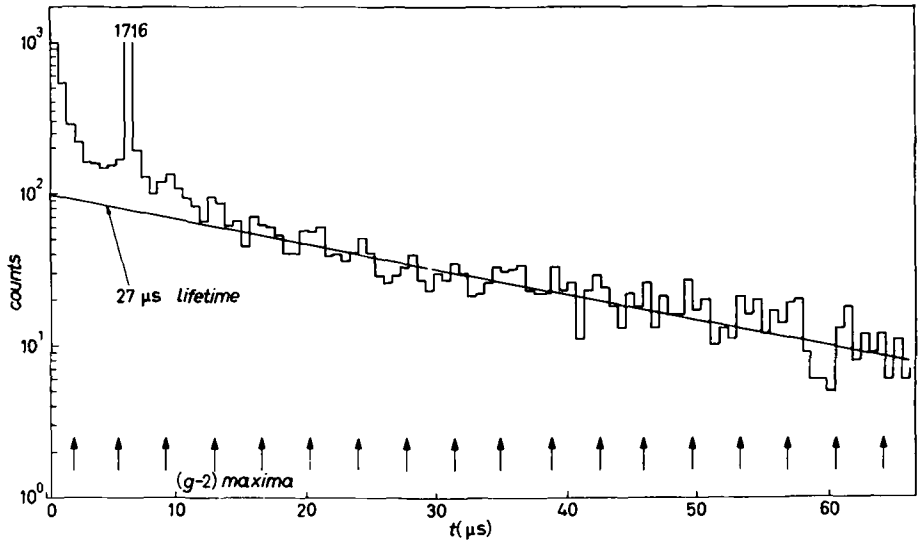

Fig. 16. – Electron counting rate *vs.* time: early data showing $(g-2)$ modulation. An intense peak is seen in the counting rate at about 6 μs due to the fact that a pulsed sweeper magnet installed in the beam line was not used: $E_e = 750$ MeV, 21 000 bunches, 1 counter.

to the Q-value of the proton synchrotron ($Q = 6\frac{1}{4}$); protons which have been kicked into oscillation by the ejection kicker, but have just missed the ejection channel, have a chance of hitting the kicker magnet three turns later and scattering into the ejection channel. The effectiveness of the sweeper magnet in eliminating background of this type is clear from Fig. 17. All data runs were taken with the sweeper magnet on.

5·4. *Storage of electrons.* – Electrons are produced in the primary target by the intense flux of γ-rays originating mainly from π^0 decay. Those with 1.3 GeV/c momentum can circle the ring, but the orbit radius decreases by 0.2 mm per turn owing to synchrotron radiation. As a result, some electrons miss the target on the first and subsequent turns, and are stored in the ring. As the orbit continues to shrink, these electrons eventually hit the inside wall of the vacuum chamber and may be scattered into the counters giving background counts. The time at which this happens depends on the amplitude of the horizontal betatron oscillation, but cannot be more than 2.5 μs × × (horizontal aperture in cm), that is 20 μs for our final configuration. Figure 18 shows the background due to this effect with a strong 14-turn modulation due to the horizontal betatron oscillations. As $Q_h = (1-n)^{\frac{1}{2}} = 0.93$, the trajectory in the horizontal plane repeats almost exactly after 14 turns, bringing the electrons again to the same point on the inner wall of the vacuum chamber.

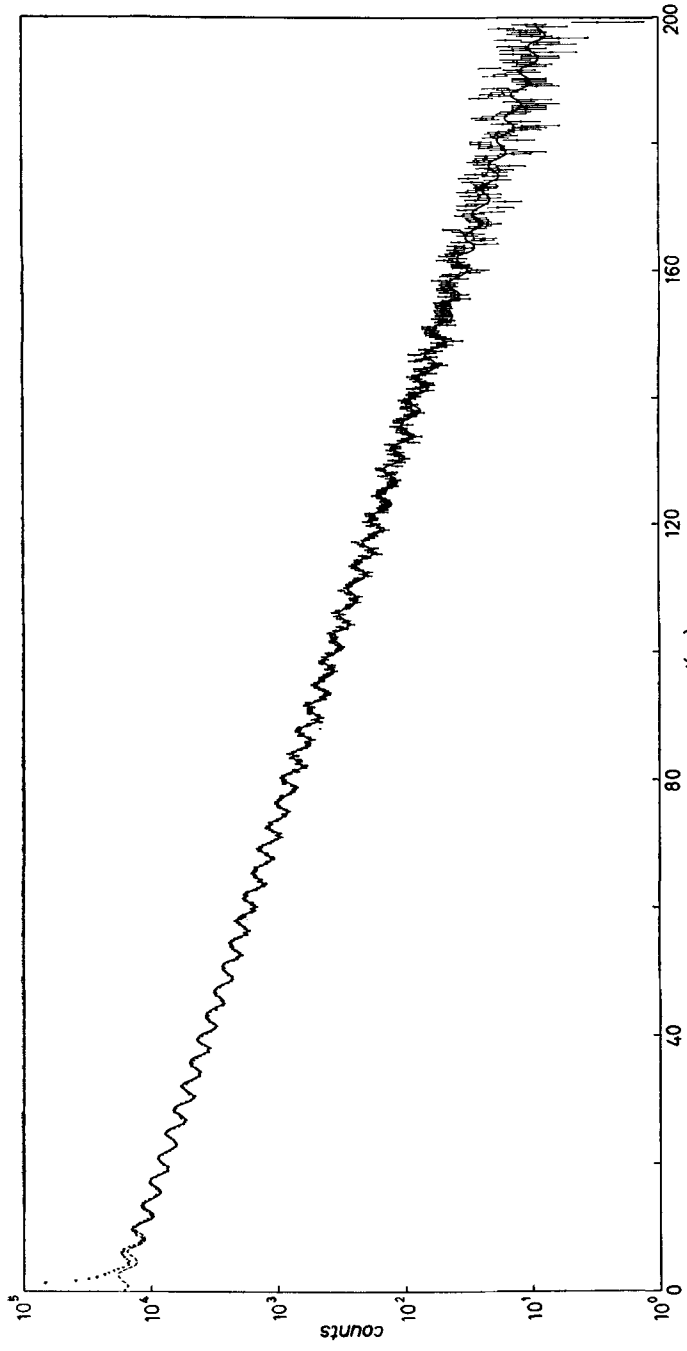

Fig. 17. – Decay electron counts modulated by the $(g-2)$ frequency of the muons. The data runs were taken with the sweeper magnet on.

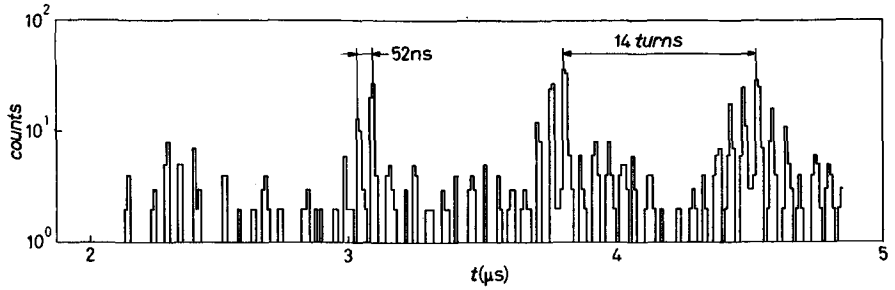

Fig. 18. – Counts due to stored electrons at an early stage of the experiment showing betatron oscillations. The horizontal betatron wavelength is such that the electrons repeat approximately the same trajectory (in the horizontal projection) every 14 turns. Thus, if the counts are due to scattering by a localized discontinuity, the rate will show a 14-turn modulation.

In order to study the muon rotation frequency at early times it was important to eliminate the stored-electron signal. We attempted to achieve this by two complementary methods:

i) We prevent electrons from being injected by mounting a 3 cm long × ×2 mm wide lead block (called the scraper) about 1 m upstream from the target, where it cannot be hit by the proton beam; its inner edge (*) is at radius 2533 mm, compared to the inner edge of the target, at 2539 mm radius.

As the electrons can only spiral inwards 2.8 mm in 14 turns (the repeat period of the horizontal trajectory) they should be largely intercepted by the scraper. Later this was supplemented by a copper scraper on the opposite side of the ring, 10 cm long × 1.5 cm radially, its inner edge at radius 2532 mm. The relative radii of the target and scraper were varied to study the influence of this distance on the counting rate at early times.

ii) When the electrons finally hit the inner wall of the vacuum chamber, we arrange that they cannot be scattered into the counters; so even if an electron is stored, it cannot give any background counts. This is achieved by placing a lead block 20 cm long × 2.5 cm wide inside the vacuum chamber, just after the counters, its outer edge being at radius 2454 mm. Most electrons will be completely absorbed inside the block; those that escape will have low energy and will be absorbed in the concrete shielding inside the ring, near the target.

5·5. *Multibunch injection.* – As previously mentioned, the diameter of the ring was chosen in such a way that the rotation period of the muons (52.5 ns) was just half the interval between proton bunches in the PS. Thus, if several

(*) All radii have been corrected for distortion of the closed orbit.

bunches were ejected, the muons generated would be superposed in the muon storage ring and the rotation frequency could still be observed. We ran with up to five PS bunches, but as this aggravated the electronic effects on the counters (see above), most of the data were taken with two or three bunches.

To obtain very clean data at early times, we ran for a short time at greatly reduced intensity, using one bunch with an absorber in the beam near the PS to reduce the proton flux by scattering (see Subsect. 6·2.2).

5·6. *Extra-counts at early times and losses.* – One expects the population of stored particles to decrease rapidly during the first few turns, owing to collisions of the rotating and oscillating particles with the limiting stops of the storage aperture. In an ideal magnetic field, the muon population has largely stabilized after 14 turns (the repeat period of the horizontal oscillations), but about 6 % further losses occur between 1 and 5 μs owing to delayed scraping of the beam. However, the observed counting rate shown in Fig. 19 shows a loss of counts of nearly a factor 2 during the first few microseconds. This loss appears to continue at a lower level for the whole storage period, as evidenced by the measured muon lifetime, which is ~1 % shorter than that predicted by special relativity (see below).

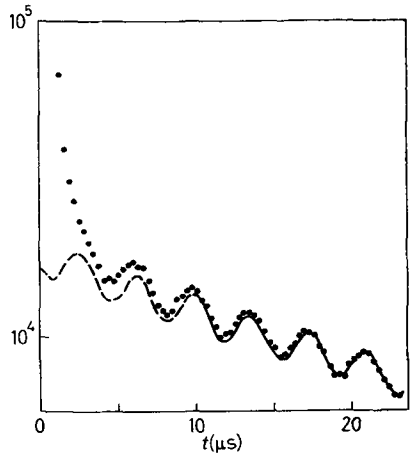

Fig. 19. – Excess of counts at early times. The fitted curve from 20.5 μs to 189 μs has been extrapolated back to compare the corresponding counting rate at early times with the experimental data.

The extra-counts may be due to any one, or a combination, of the following effects:

i) perturbation of the electronics at early times by the initial flash or the protective blanking, or pile-up of background pulses;

ii) extra particles which either decay (heavy muon) or hit the walls (stored electrons);

iii) a genuine loss of muons.

We believe that all three effects contribute. At the normal intensity a continuous background is seen at early times. This disappears when we run at reduced intensity (see Subsect. **6**·2.2 and Fig. 23 mentioned therein), and for example the extra count factor at 3 μs is reduced from 1.4 to 1.25. So about 15% of the extra-counts at 3 μs are due to pile up.

Considerable effort was devoted to an *a posteriori* analysis of the extra counts data after 5 μs. When a double decay function was fitted to the data, one function corresponded to the muon signal in lifetime, asymmetry, etc.; the other showed a lifetime of about 12 μs, and had no significant modulation at the $(g-2)$ frequency. This latter component could be compatible with the presence of stored electrons (which were stored despite the precautions described in Subsect. **5**·4 above) or with counting pile-up effects.

On the other hand, the continuing small loss of $\sim 1\%$ per muon lifetime (seen in both low- and high-intensity runs) cannot be due to stored electrons. We understand this loss as an effect of imperfections in the magnetic field. These can excite both horizontal and vertical oscillations, which can bring a particle into collision with the vacuum chamber after many hundreds of orbits. An analytical treatment of nonlinear resonances shows that losses of about $\sim 1\%$ per lifetime can be expected (see Appendix C). The implications of these losses for the assessment of the mean radius of the rotating muons via the observed rotation frequency is discussed in Sect. **6**. Experiments which show that the loss is symmetric in the aperture are described at that point.

It can be shown that losses due to single or multiple scattering of muons by molecules of the residual gas in the vacuum chamber are four orders of magnitude too small to explain the observed losses.

5·7. *Data-taking runs.* – The data used to calculate a_{exp} were taken in seven separate runs, three devoted to μ^+ and four to μ^-, as indicated in Table IV, which also shows the times when the magnet was remeasured. Small variations of aperture and counter arrangement were made from time to time to improve the running conditions.

During all these runs the magnetic field was measured continuously by the stabilizer probe, and checked every 4 min by the four monitor probes. Routine checks were made to ensure that the electronics were working correctly.

After every PS pulse, the following data were written on magnetic tape: the run number and date, the encoded proton beam intensity, the positions of the four moving magnetic probes, whether all five magnetometers were correctly locked, the five proton resonance frequencies, all digitron scaler

TABLE IV. – *Summary of individual runs.*

Run [a]	Charge of muon	Total decay electrons recorded	Mean radius $\bar{\varrho}$ [b] (mm)	$\bar{\omega}_p$ [b] (MHz)	τ_{th} [b] (μs)	τ_{exp} [b] (μs)	ω_a [b] (MHz)	$a \times 10^{-8}$
* 9 *	—	989 k	2494.4	72.8150	26.69	26.40 ± 0.06	1.69645	116627 ± 30
* 10	+	42 k	2491.8	72.8245	26.67	27.51 ± 0.49	1.69408	116484 ± 180
11	+	297 k	2493.7	72.8185	26.69	26.22 ± 0.05	1.69604	116593 ± 80
12 *	+	13 k	2494.7	72.8152	26.70	26.57 ± 0.56	1.69734	116688 ± 390
* 13	—	392 k	2492.7	72.8186	26.68	26.47 ± 0.04	1.69682	116646 ± 48
14	—	200 k	2494.3	72.8117	26.69	27.55 ± 1.46	1.69475	116515 ± 75
15 *	—	41 k	2494.0	72.8083	26.69	27.27 ± 0,37	1.70060	116923 ± 179

(*a*) The asterisks * indicate a magnetic field survey before or after the run.
(*b*) $\bar{\varrho}$ is obtained by fitting the rotation frequency data at early times, ω_p is the average proton resonance frequency for the run corrected for $\bar{\varrho}$, τ_{th} is obtained from eq. (25), τ_{exp} and ω_a are obtained by fitting eq. (14) to the data, and a is then calculated from eq. (4). The errors are statistical only.

readings, and digitron overflow indicators. The correct tracking of the magnetometer servo-circuits was checked regularly by means of an oscilloscope display (see Sect. **2**). Similar data were transferred to the on-line PDP-8, but this was used only for monitoring the runs.

6. – Data analysis.

6·1. *General criteria for data analysis.* – All analysis is made from the data recorded on magnetic tape. The first process is to assemble the digitron readings into a histogram of counts *vs.* time, while entirely rejecting any PS cycles which do not satisfy the following criteria:

i) ejected proton beam above a certain threshold;

ii) magnetometers in lock mode, and frequencies within prescribed limits;

iii) digitron scaler readings increase progressively;

iv) digitron scalers which have not been stopped by decay electrons read the correct final stop number;

v) no digitron overflow;

vi) if digitron is split, the corresponding scalers in the two halves agree exactly.

If all these conditions are satisfied, two histograms are constructed by adding 1 to the channel address specified by each scaler reading: *a*) the fast

histogram, 5 ns per channel, covering 0 to 10 μs, used for finding ω_r; *b*) the slow histogram, 105 ns per channel, covering 0 to 300 μs, used for finding ω_a: by summing over 21 adjacent fast channels the rotation frequency signal is eliminated to first order.

At the same time the proton resonance frequency, given for each pulse by the stabilizer probe, is weighted according to the number of observed decay electrons and averaged to give the mean value $\bar{\omega}_{stab}$ for the run.

Every hundred pulses, the four moving magnetometers are driven pneumatically to radius 2500 mm, nearly the centre of the storage aperture. On these occasions, all five magnetometer readings are available, and one can calculate the average monitor frequency ω_{mon} and compare it with ω_{stab}. The mean value of $\Delta\omega = (\omega_{mon} - \omega_{stab})$ is evaluated for the run, so finally the mean monitor frequency $\bar{\omega}_{mon}$ corresponding to each run can be determined: $\bar{\omega}_{mon} = \bar{\omega}_{stab} + \overline{\Delta\omega}$.

The next task is to fit the electron counting data to obtain the mean radius of the ensemble of muons, and to find $\bar{\omega}_a$.

6·2. *Measurement of mean radius of the muon sample.* – As pointed out in Sect. **2**, the proton resonance frequency was mapped to ~10 ppm at many specified points throughout the storage volume, but the magnetic field varied by 2100 ppm in passing from the inner to the outer wall, because of the gradient necessary for vertical focusing. For an exactly linear gradient the mean field depends only on the mean radius of the ensemble of muons. This mean radius has been determined to about 7 % of the aperture half-width, reducing the uncertainty from this source to less than the statistical error in the $(g-2)$ frequency. The methods used for doing this and several experimental checks are as follows.

6·2.1. Rotation frequency fitting method. Since muons are released in the storage ring in a time (~10 ns) shorter than their revolution time (~52.5 ns), the sample at first rotates as a distinct bunch, and this structure is reflected in the time distribution of the decay electrons which are detected. However, the low-momentum muons have a shorter rotation period than the high-momentum muons, so the bunch begins to overlap itself (after about 1.5 μs) and eventually the structure disappers. This rotational structure is the basis of the primary method of finding the mean radius, since the rotation period $T = 2\pi\varrho_e/\beta c$ of a given muon is given essentially by its equilibrium radius ϱ_e, with negligible corrections for betatron oscillations (see Subsect. **6**·3 below).

Decay-electron arrival times are sorted into a histogram of 5 ns bins. Figure 20 shows the data, collected from several runs, for the first few microseconds. The very high background rates which occur immediately after the proton beam strikes the target in the storage ring make it difficult to get a

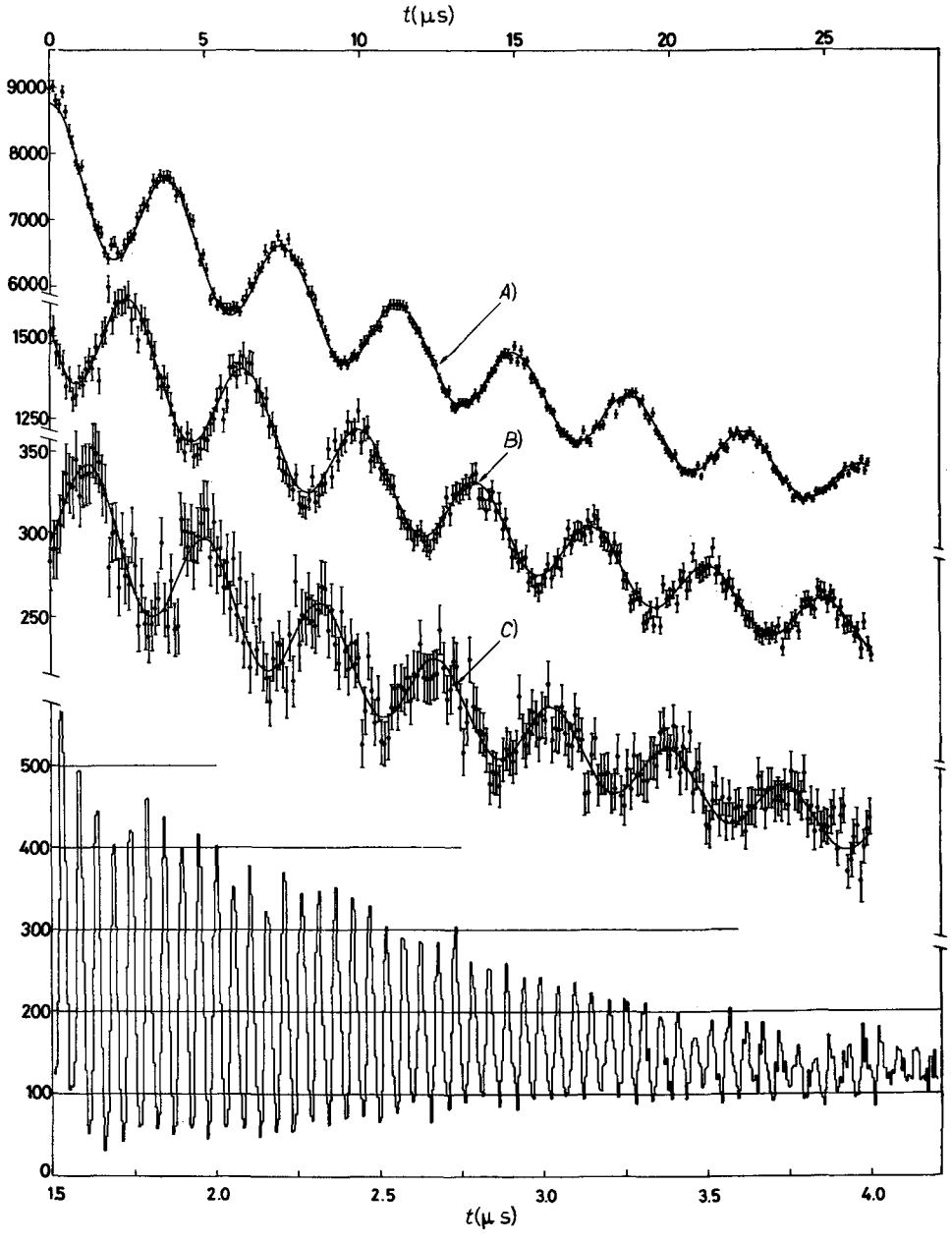

Fig. 20. – Distribution of decay electrons as a function of time. *A*) from 20 to 45 μs, *B*) from 65 to 90 μs, *C*) from 105 to 130 μs (upper scale of time). The lower curve shows the rotation frequency of the muon as seen at early times: lower scale of time. To obtain ω_a a maximum likelihood fit to the data is made with eq. (14). Data are fitted from 20.5 μs to 189 μs.

clean signal until about 1.5 μs after injection under normal conditions. Also, the muon sample at the start contains particles which will eventually hit the walls. We must therefore extract the muon distribution from the somewhat diluted data of the spread out, partially overlapping bunch. This is done by a fitting program. The program attempts to fit the observed histogram by calculating the counting-rate pattern generated by an assumed distribution of muon equilibrium radii. The distribution is described by the populations of ten overlapping radial bins. It is continuous, with discontinuous derivatives, and falls to zero at the prescribed boundaries. The minimum-chi-squared problem is solved for the nine relative populations and for the injection time. The initial time distribution of the injected proton bunch is normally assumed to be a square pulse 10 ns long.

In the interval in which the fitting is done (generally 1.5 to 5.5 μs) some background is still present. For this reason, and also because of the simplifying assumptions such as square initial bunch width, a perfect fit would not be expected, and indeed there are deviations especially at early times.

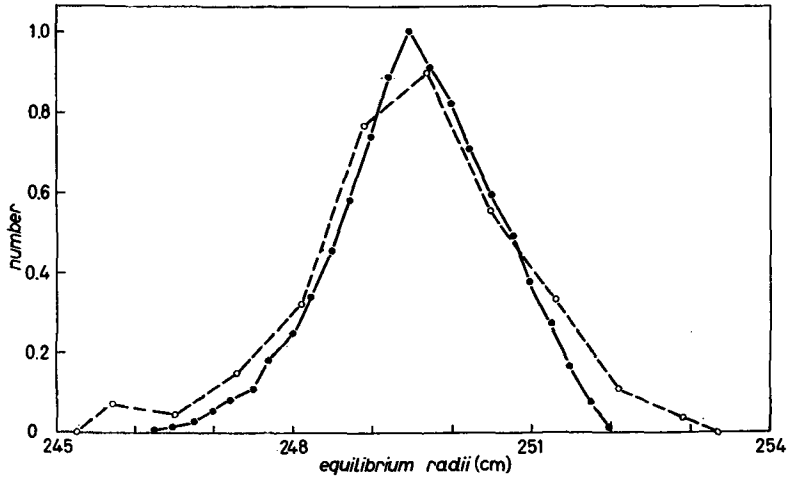

Fig. 21. – Muon radius distribution derived from the analysis of the decay-electron events at early times. The muon rotation frequency has been analysed from 1.8 μs to 5.5 μs: – – – muon distribution derived from rotation frequency, ——— predicted muon distribution.

Figure 21 shows the resulting radial distribution. It is reasonable, and the muon population agrees with what one expects on physical grounds, as indicated in Subsect. 1·1 and Appendix A. From the statistics of the input data, one would expect, with a correct hypothesis, a determination of the mean radius to better than one millimetre. We expect the true situation to be worse, since the hypothesis cannot be exact. To extract a more realistic error estimate from the program we have made two investigations:

i) A number of changes in the assumptions of the fitting program were tried to see whether the resulting mean radius is stable against such changes. For example, the time distribution of the sample at input was changed, both in width and in shape, the positions of the boundaries of the trapping volume were altered, the number of radial bins was changed, the interval over which the fitting was done was varied, and an adjustable amount of background (unmodulated signal) was subtracted. Such changes, if reasonably small, did not generally change the mean radius by more than ± 2 mm.

ii) Artificial data were generated by a Monte Carlo program and then put through the fitting program. In this way many potentially trouble-making situations were explored, such as the effect of nonrotating background, of non-square-wave input pulse (we used a Gaussian), of slow variation of intensity, and of very asymmetric distributions. The results are summarized in Table V; the fitted mean radius is always correct to a few millimetres, but the deviation from the input mean radius is, as expected, more than purely statistical.

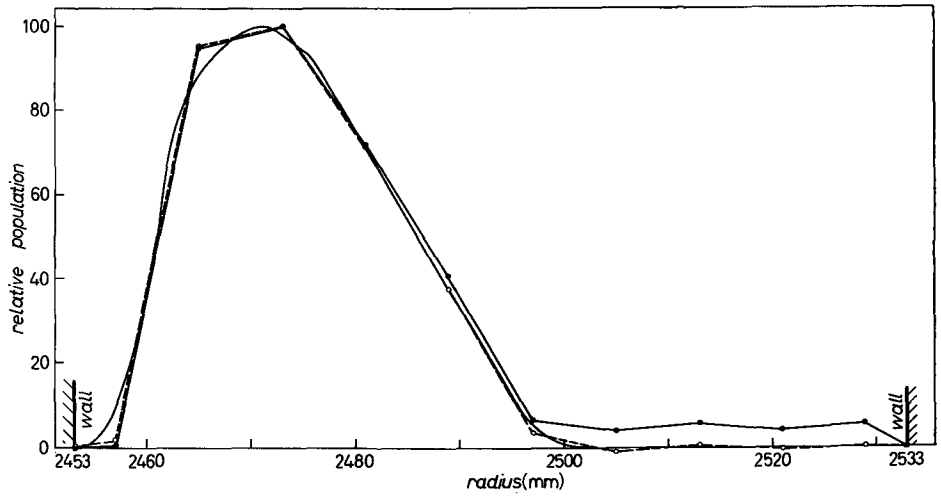

Fig. 22. – Fitting results for two unfavourable cases: *a*) a very asymmetric distribution which had a Gaussian-shaped initial time distribution, and *b*) the same with background present: ——— input $\bar{R} = 2474.41$ mm; ——o—— no background, distribution found by fitting, $\bar{R} = 2474.48$ mm; ——•—— with background, distribution found by fitting, $\bar{R} = 2477.52$ mm.

Figure 22 shows the fitting results for two unfavourable cases—a very asymmetric distribution which had a Gaussian-shaped initial time distribution, and the same with background present. The fit is remarkably good. The presence of nonrotating background is seen to cause the addition of a spread-out muon distribution, which in turn moves the mean radius toward the centre

if the true distribution is asymmetric. In this case the effect was 3.1 mm out of 19 mm; in the six runs of Table V case *c*) it averaged 2.1 mm out of 4.5 mm.

In the actual experiment the mean radius was found to be only 1 mm from the geometrical centre of the storage volume. Thus the true distribution must have a mean radius near the centre, and the systematic effect must be less than the random error of 2 to 3 mm.

TABLE V. – *Summary of some Monte Carlo tests of the accuracy of mean-radius location by the fitting program.*

Test	r.m.s. deviation from input radius (mm)	Remarks
a) Distribution far off-centre (19 mm), no background	0.05	
b) Same, with background	3.11	Background causes a systematic shift toward the centre
c) Distribution similar to that observed in the experiment, but off-centre by 4.5 mm. Realistic input pulse and background, 6 runs	2.20	Average shift toward the centre was 2.1 mm
d) All reasonable runs, various distributions, background and input pulse conditions, 31 runs	2.7	The worst case was 5 mm off

From these studies it appears that a conservative error to assign to the mean-radius determination by the fitting method is 2.7 mm.

The mean radius was calculated in this way for all runs with the results given in Table IV. We calculated the mean field $\bar{B}$ from these data, but made several further checks to establish its validity.

6·2.2. Direct measurement at low intensity. During part of Run 14 the intensity was deliberately cut by a factor of 5 by putting an absorber in the proton beam near the PS. This removed the nonrotating background which is usually present at early times, and which we assume to be caused by pile-up of small background counts. This clean signal (Fig. 23) allows a direct determination of the mean rotation frequency and therefore mean radius, in the time ($(0.6 \div 1.6)\,\mu$s) before the bunch begins to overlaps itself. The error is given by the counting statistics. Data for this run are given in Table VI, where it can be seen that within the statistical error of the direct determination (± 2.1 mm) it agrees with the mean radius from the fitting method both at the lower intensity and at normal intensity.

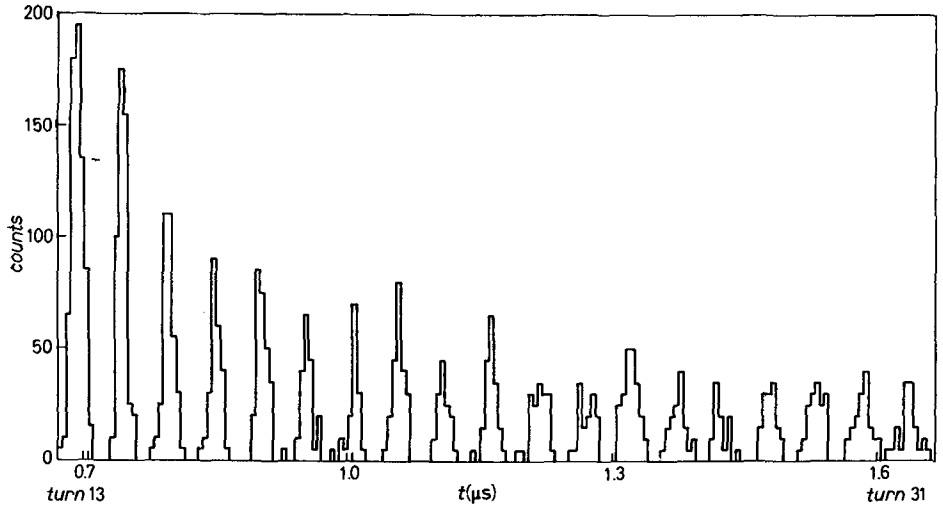

Fig. 23. – Reduced-intensity experiment. The muon rotation frequency using one-fifth of one-bunch intensity. The analysis of the data has been done, starting from 0.6 μs to 1.6 μs, *i.e.* before the muon bunch overlapped itself.

Direct observation also yields T_0', the centroid of the injection time. This is a fitted parameter in the fitting method; it is gratifying that the two values agree to 2 ns.

TABLE VI. – *Mean radius measurements.* The standard method of analysis is compared with the direct analysis for rotation frequency at early times with reduced intensity. The centre of the aperture is at radius 2493 mm.

Method	Excess count factor	Mean radius (mm)	Remarks
Standard method, full intensity (1.8÷6.0) μs	1.4 at 2.5 μs	2494.3±2.7	Systematic error from Monte Carlo studies
Standard method, reduced intensity	1.25 at 2.5 μs	2492.4±2.8	Error from statistics; this is now comparable with systematic error
Direct rotation frequency, reduced intensity, (0.6÷1.6) μs	3.0 at 1 μs	2492.5±2.1	Error from statistics

6·2.3. Change of radius with time. The radius obtained from the rotation frequency applies to the particle population present at about 3 μs after injection. However, the $(g-2)$ precession is measured over a later period, (20.5÷189) μs, and we have already discussed in Subsect. 5·6 the 25% loss of particles which occurs between these two periods. As a result, the mean

radius of the muon population at late times may not be the same as that measured at 3 μs. In the worst case, if 25 % of the radial distribution of Fig. 21 were cut off on one side, the mean radius would change by 6 mm.

To study this question we have obtained supplementary information by restricting the horizontal aperture from the inside and from the outside of the ring. The stops are so placed that they are unlikely to be hit by pions which could usefully inject a muon into the available aperture afterwards. It is assumed that the reduction in stored intensity is due to the elimination of muon orbits which intersect the stop.

Let the number of decay electrons observed in a particular time with the unrestricted aperture ($\pm a$) be I_0, and let the corresponding intensities when the aperture is reduced by $0.5a$ from the inside and outside separately be I_- and I_+. Then for all reasonable radial distributions and oscillation amplitudes the mean radius is

$$\bar{\varrho} = \varrho_0 + Ca(I_- - I_+)/I_0 , \tag{13}$$

where the numerical constant C is 0.5 within a factor of 2. The results are given in Table VII.

TABLE VII. – *Data for run* 14. The centre of the aperture was at radius 2492.5 mm.

Residual total aperture (cm)			Intensity	
			Early (2.3÷3.4) μs	Late (20.7÷39.9) μs
Full	7.9	I_0	8.3	19.54
Stop on inside	5.9	I_-	2.68	6.36
		(I_-/I_0)	(0.321)	(0.325)
Stop on outside	6.5	I_+	3.95	9.44
		(I_+/I_0)	(0.474)	(0.482)

As the change in aperture was not the same in the two cases, it is necessary to plot I *vs.* (aperture)^2 to establish that blocking on the inside or the outside gives the same effect to ±10 %. The uncertainty comes from the 1 mm uncertainty in the position of the stops. Applying eq. (13), we then find for *late times only*:

Run 14: $\bar{\varrho}$(late) = (2492.5 ± 1.0) mm,

Run 15: $\bar{\varrho}$(late) = (2494.3 ± 1.0) mm,

agreeing with the values obtained for early times by the fitting method (Table IV).

A more precise statement can be made about the change of radius with time by comparing (I_-/I_0) for late and early times for the same runs, and similarly for (I_+/I_0). This is independent of our exact knowledge of the position of the stops, and drifts in the monitor. This gives

$$\begin{aligned}\Delta\varrho &= Ca\left[\left(\frac{I_-}{I_0}\right)_{\text{early}} - \left(\frac{I_-}{I_0}\right)_{\text{late}} - \left(\frac{I_+}{I_0}\right)_{\text{early}} + \left(\frac{I_+}{I_0}\right)_{\text{late}}\right], \\ &= (0 \pm 1)\,\text{mm (run 14)}, \\ &= (+2.1 \pm 1)\,\text{mm (run 15)}.\end{aligned}$$

Furthermore, from Table VI, there is no significant change of radius between 1 and 3 μs in spite of the large drop in extra counts. Therefore, it is unlikely that the radius changed appreciably at later times.

In summary, three independent methods of finding the mean radius agree, and we have evidence that the change of radius with time is small. Taking into account the redundancy of the data, we adopt conservatively an error of ±3 mm in mean radius for all runs. This contributes an error of 160 ppm in the value of a.

6·3. *Determination of* $(g-2)$ *precession frequency* ω_a. – The modulation of decay-electron counting rate by the $(g-2)$ precession is clearly seen in the data (see Fig. 20). To obtain ω_a, a maximum likelihood fit to the data is made with the following function:

$$(14)\quad N(t) = N_0 \exp[-t/\tau](1 + E\exp[-t/\tau_e])\{1 - A\cos(\omega_a t + \varphi)\} + B_g.$$

Here the symbols N_0, τ, A, ω_a and φ have the same meaning as in eq. (2), but the parameters E and τ_e have been added to take account of the extra-counts at early times. B_g is added to include a possible constant background. The fitting programme was carefully checked with artificial data, and also shown to give results which are independent of small variations in the time interval selected for fitting (*); a is calculated via eq. (4) with $\lambda(1+\varepsilon) = = 3.18342$.

The values obtained by adjusting the eight parameters in eq. (14) are given in Table IV for seven separate runs fitted from 20.5 to 189 μs. The error quoted here on a includes only the statistical error in the maximum likelihood adjustment. The seven values agree well with each other, giving $\chi^2 = 6.17$.

(*) In previous publications [3,4] we reported ω_a-values obtained from a five-parameter fit using eq. (2) which does not allow for the extra-counts. In this case the value of ω_a depends slightly on the starting point of the data selected for fitting. In particular, the value of a reported in 1967 was later found to be too high because of this effect.

For 6 degrees of freedom the expected value is 5.4, and the probability of finding 6.17 or more is 42%.

The weighted mean value of the anomalous moment is

$$a = (116\,621 \pm 23)\cdot 10^{-8}. \tag{15}$$

The error of the mean is $23\cdot 10^{-8}$, but this should be increased by $(6.17/5.4)^{\frac{1}{2}}$ to take account of the unknown random errors which have apparently intervened to make χ^2 slightly larger. (In effect, we calculate the error from the spread of the data in Table IV.) This brings the random error to $25\cdot 10^{-8}$ (215 ppm).

We now add in quadrature the error corresponding to a ± 3 mm uncertainty in mean radius discussed above, which is $19\cdot 10^{-8}$ (160 ppm), to give the final overall error, $31\cdot 10^{-8}$ (270 ppm).

Corrections. We must also consider a number of small corrections to the result, as follows:

i) Due to the slight nonlinearity of the field B *vs* radius ϱ, the field $\bar{B}$ averaged over a distribution of equilibrium orbits differs slightly from the field $B(\bar{\varrho})$ at the average radius of that distribution. If the muons populate the available phase space uniformly,

$$\frac{\Delta B_1}{B} = \frac{B - B(\bar{\varrho})}{B} = -\frac{1}{20}\frac{a^2}{\varrho_0^2}\varrho_0 \cdot \frac{\mathrm{d}n}{\mathrm{d}\varrho} = +25 \text{ ppm}, \tag{16}$$

where ϱ_0 is the radius at the centre of the aperture.

A calculation using the actual field map and a theoretical orbit distribution gave $+34$ ppm which we adopt.

ii) *Vertical oscillations* of the particle about the median plane have three effects:

a) an increase in $\bar{B}$, because the field near the poles is greater than in the median plane. This is proportional to $\mathrm{d}^2B/\mathrm{d}z^2$ $(= -\mathrm{d}^2B/\mathrm{d}\varrho^2)$;

b) a slowing down of the rotation frequency due to the longer path;

c) the pitch correction ([14]) to the spin motion which in effect reduces $\bar{B}$ by the factor $(1 - v_z^2/c^2)^{\frac{1}{2}}$.

For vertical semi-aperture b, and a muon population which fills the vertical phase-space uniformly, we find that the magnetic field obtained from the rota-

([14]) G. R. HENRY and J. E. SILVER: *Phys. Rev.*, **180**, 1262 (1969).

tion frequency must be further corrected as follows:

$$\frac{\Delta B_2}{B} = \frac{1}{8}\left(\frac{b}{\varrho_0}\right)^2 \left\{\varrho_0 \frac{\mathrm{d}n}{\mathrm{d}\varrho} + n^2 - n\right\}, \tag{17}$$

where the three terms correspond, respectively, to *a*), *b*) and *c*) above. With $b = 2.1$ cm, $n = 0.13$ and $\varrho_0(\mathrm{d}n/\mathrm{d}\varrho) = -2.2$, the three terms give respectively -19.8, $+0.15$ and -1.2 ppm corrections.

iii) *Horizontal oscillations* of the particle about its equilibrium orbit may be analysed as follows. For a particular equilibrium orbit $\varrho_\parallel$, let the oscillation in radius be described by ϱ_1 so that $\varrho = \varrho_\parallel + \varrho_1$. Expanding the field about $\varrho_\parallel$, we get

$$B(\varrho) = B_\parallel + \varrho_1 B' + \tfrac{1}{2}\varrho_1^2 B'',$$

where $B_\parallel = B(\varrho_\parallel)$, $B' = \mathrm{d}B/\mathrm{d}\varrho = -nB_0/\varrho_0$ and $B'' = \mathrm{d}^2B/\mathrm{d}\varrho^2 = -(B_0/\varrho_0)\mathrm{d}n/\mathrm{d}\varrho$. Then

$$\bar{B} = B + B'\bar{\varrho}_1 + \tfrac{1}{2}B''\overline{\varrho_1^2}. \tag{18}$$

In addition, the oscillation changes the rotation frequency, particularly if the oscillation is nonlinear ($B'' \neq 0$):

$$\dot{\theta} = \beta c/\varrho = (\beta c/\varrho_\parallel)(1 - \varrho_1/\varrho_\parallel + \tfrac{1}{2}\varrho_1^2/\varrho_\parallel^2).$$

On averaging over many orbits to get ω, this gives an apparent radius

$$\varrho_{\mathrm{app}} = \varrho_\parallel + \bar{\varrho}_1 + \frac{1}{2\varrho_\parallel}\{(\bar{\varrho}_1)^2 - \overline{\varrho_1^2}\},$$

so the field is apparently

$$B_{\mathrm{app}} = B_\parallel + B'\bar{\varrho}_1 + (B'/2\varrho_\parallel)\{(\bar{\varrho}_1)^2 - \overline{\varrho_1^2}\} + \tfrac{1}{2}B''(\bar{\varrho}_1)^2, \tag{19}$$

giving

$$\frac{\bar{B} - B_{\mathrm{app}}}{B} = -\frac{\overline{\varrho_1^2} - (\bar{\varrho}_1)^2}{2\varrho_\parallel^2}\left\{n + \varrho_\parallel \frac{\mathrm{d}n}{\mathrm{d}\varrho}\right\}.$$

For an oscillation of amplitude A, $\overline{\varrho_1^2} = \frac{1}{2}A^2$, while $\bar{\varrho}_1 \sim 0$. To estimate A^2 we assume that the available horizontal phase space is uniformly populated with muons, and then make the weighted average over all available values of $\varrho_\parallel$. For horizontal semi-aperture a, $\bar{A}^2 = 0.3a^2$, so finally

$$\frac{\Delta B_3}{B} = \frac{\bar{B} - B_{\mathrm{app}}}{B} = -\frac{3a^2}{40\varrho_0^2}\left\{n + \varrho_0 \cdot \frac{\mathrm{d}n}{\mathrm{d}\varrho}\right\}. \tag{20}$$

With $a = 3.8$ cm, $n = 0.13$ and $\varrho_0 dn/d\varrho = -2.2$, this gives a correction of $+35.9$ ppm.

The effect of vertical and horizontal oscillations on $(\bar{B} - B_{app})$ has also been evaluated by a computer simulation of the particle orbits in the measured field of the magnet. In a step-by-step integration, the orbit is followed for ~ 10 turns (a whole number of horizontal oscillations), and the true $\bar{B}$, and B_{app} calculated from the rotation frequency, are evaluated. Including both horizontal and vertical oscillations, this gives an average correction to $\bar{B}$ of $+29$ ppm, agreeing reasonably well with the net oscillation correction of $+15$ ppm estimated above. The computed shift also takes into account the effect of noncircular equilibrium orbits on $\bar{B}$, and so we adopt $\Delta B_2 + \Delta B_3 = +29$ ppm.

iv) *The change of radius*, due to the dependence of the muon lifetime on radius, gives after time t a relative change in $\bar{B}$ of $-n(t/\tau)[\overline{(\varrho_1 - \varrho_0)^2}/\varrho_0^2]$. With the distribution of equilibrium radii of Fig. 21, $\overline{(\varrho_1 - \varrho_0)^2} = 2$ (cm)^2. Also it can be shown that the weighted average age of the muons which contribute to the measurement of ω_a is $3\tau/2$ after the start of the analysis (20.5 μs). Thus $t/\tau = 2.2$. The correction is $\Delta B_4 = -9$ ppm.

v) We must now consider the 1% loss of particles per muon lifetime, which continues throughout the period used for fitting the $(g-2)$ frequency (see eq. (26) below). This could give rise to a progressive change of phase φ in eq. (14), and so lead to an error in the fitted frequency. The initial phase of the ensemble of muons which contribute to the data includes the mean muon spin direction (referred to time zero) together with the mean emission angle θ_{eff} in the muon rest frame of the detected electrons. If some muons are lost, these mean values can change.

We estimate from Figs. 2 and 21 that a 1% loss of muons could change the mean radius by at most $4 \cdot 10^{-2}$ cm, and the muon spin angle by at most 0.6 mrad. A progressive phase shift of this magnitude every 27 μs would change ω_a by 12 ppm. Calculations of the electron trajectories from muons at different radii show the change in θ_{eff} with muon radius is negligible. Hence, if the losses correlate with radius, the maximum correction to ω_a is 12 ppm, which can be neglected.

All these corrections are small, and we know of no other which can significantly affect the result. The combined correction from i), ii), iii) and iv) is $+54$ ppm in B. Therefore, if we apply a correction of -54 ppm to eq. (15), the final result of the experiment is

$$a_{exp} = (116\,616 \pm 31) \cdot 10^{-8}. \tag{21}$$

7. – Comparison with theory.

The anomalous moment of the muon at the new level of accuracy is influenced by many small effects. As a result, the theoretical value has been evolving, both during the experiment and after, as detailed for example in recent review articles ([15,16]). For quantum electrodynamics alone the prediction is

$$(22) \qquad a_{\text{theory}}^{\text{QED}} = \alpha/2\pi + 0.7658\alpha^2/\pi^2 + (21.8 \pm 1.1)\alpha^3/\pi^3 = (116\,581 \pm 1.4)\cdot 10^{-8},$$

where the fine-structure constant α is taken ([16]) as $\alpha^{-1} = (137.03608 \pm 1.9)$ ppm.

In eq. (22) it is assumed that the electrodynamic coupling of the muon is identical to that of the electron. The fourth-order α^2-term ([17]) includes the effect of electron loop insertion in the second-order muon vertex ($1.0943\alpha^2/\pi^2$) which augments the anomalous moment of the muon relative to the electron. The sixth-order term consists of: *a*) an estimate of the coefficient which is valid for both electron and muon, $0.55\alpha^3/\pi^3$, obtained from two specifically calculated terms ([18,19]) plus a dispersion-theoretical estimate of the others ([20]) ($0.13\alpha^3/\pi^3$); and *b*) the effect of inserting electron loops in second-order and fourth-order diagrams which makes a_{theory} different from that of the electron. All terms in *b*) have now been calculated ([21]), including the photon-photon scattering diagrams ([19]) which contribute $(18.4 \pm 1.1)\alpha^3/\pi^3$. This last, surprisingly large term was only known in 1969, after our result (eq. (21)) had been published, and has brought the theory into accord with our measurements (*).

([15]) J. BAILEY and E. PICASSO: *Progr. Nucl. Phys.*, **12**, 43 (1970); S. J. BRODSKY and S. D. DRELL: *Ann. Rev. Nucl. Sci.*, **20**, 147 (1970); B. LAUTRUP: *Phys. Lett.*, **32** B, 627 (1970).

([16]) B. N. TAYLOR, W. H. PARKER and D. N. LANGENBERG: *Rev. Mod. Phys.*, **41**, 375 (1969).

([17]) A. PETERMAN: *Helv. Phys. Acta*, **30**, 407 (1957); *Fortschr. Phys.*, **6**, 505 (1958); H. SUURA and K. WICHMANN: *Phys. Rev.*, **105**, 1930 (1957); C. M. SOMMERFIELD: *Phys. Rev.*, **105**, 1931 (1957).

([18]) J. A. MIGNACO and E. REMIDDI: *Nuovo Cimento*, **60** A, 519 (1969).

([19]) J. ALDINS, T. KINOSHITA, S. J. BRODSKY and A. DUFNER: *Phys. Rev. Lett.*, **23**, 441 (1969); *Phys. Rev. D*, **1**, 2378 (1970).

([20]) S. D. DRELL and H. R. PAGELS: *Phys. Rev.*, **140** B, 397 (1965); R. G. PARSONS: *Phys. Rev.*, **168**, 1562 (1968).

([21]) T. KINOSHITA: *Nuovo Cimento*, **51** B, 140 (1967); B. E. LAUTRUP and E. DE RAFAEL: *Phys. Rev.*, **174**, 1835 (1968); *Nuovo Cimento*, **64** A, 322 (1969); B. E. LAUTRUP, A. PETERMAN and E. DE RAFAEL: *Nuovo Cimento*, **1** A, 238 (1971); B. E. LAUTRUP: *Phys. Lett.*, **32** B, 627 (1970).

(*) *Note added in proofs* (*May 1972*). – All terms in *a*) have now been calculated by M. LEVINE and J. WRIGHT (*Phys. Rev. Lett.*, **2** B, 1351 (1971)) and we have amended eqs, (22) *et seq.* accordingly. For a recent review see B. E. LAUTRUP, A. PETERMAN and E. DE RAFAEL: *Phys. Rep.*, (1972).

To the pure QED value of eq. (22) must be added the effects of inserting hadron loops into the photon propagator in the basic second-order vertex diagram. These effects are greatly enhanced by the existence of the 1^- vector-meson resonances ([22]): ρ, ω and φ. Estimates have varied in step with the experimental information on the width and strength of these states. Using the latest Orsay measurements ([23]) the contributions of the three resonances ([24]) are $(5.4, 0.61 \text{ and } 0.50)\cdot 10^{-8}$, respectively, giving a total $\Delta a^{\text{strong}} = (6.5 \pm 0.5)\cdot 10^{-8}$. It should be noted that the contribution of each hadronic state is always positive ([25]), so while the influence of massive states decrease roughly as $1/M^2$ and a significant contribution from unknown regions of the hadron spectrum is unlikely, it cannot be excluded. The rather direct connection between the hadronic part of the anomalous moment of the muon and the cross-section for e^+e^- annihilation to hadrons ([25,26]) should enable this problem to be clarified.

The influence of the weak interaction becomes significant only if it is mediated by an intermediate boson $W^{\pm}$. In this case, $\mu^{\pm}$ can turn virtually into $(W^{\pm} + \nu_{\mu})$, changing the anomalous moment ([27]) by about $-2\cdot 10^{-8}$. This is much smaller than the experimental error and may always be masked by the uncertainty in Δa^{strong}.

Adding the hadronic contribution to eq. (22) gives the current theoretical value

$$a_{\text{theory}} = (116\ 588 \pm 2)\cdot 10^{-8}. \tag{23}$$

When we completed our experiment the theoretical value was lower by $23\cdot 10^{-8}$, and we reported ([5]) a discrepancy $a_{\text{exp}} - a_{\text{theory}} = (450 \pm 270)$ ppm. Now with the calculation of the photon-photon scattering terms, the agreement has become very satisfactory. From eqs. (21) and (23) we have

$$a_{\text{exp}} - a_{\text{theory}} = (28 \pm 31)\cdot 10^{-8} = (240 \pm 270) \text{ ppm}. \tag{24}$$

This result sets limits on the various modifications to the theory of quantum electrodynamics and on new couplings which have been proposed, partly in

---

([22]) C. BOUCHIAT and L. MICHEL: *Journ. Phys. Radium*, **22**, 121 (1961); L. DURAND III: *Phys. Rev.*, **128**, 441 (1962).

([23]) J. E. AUGUSTIN, J. C. BIZOT, J. BUON, J. HAISSINSKI, D. LALANNE, P. MARIN, H. NGUYEN NGOE, J. PEREZ-Y-JORBA, F. RUMPF, E. SILVA and S. TAVERNIER: *Phys. Lett.*, **28** B, 503, 508, 513, 517 (1969).

([24]) M. GOURDIN and E. DE RAFAEL: *Nucl. Phys.*, **10** B, 667 (1969).

([25]) H. TERAZAWA: *Phys. Rev.*, **177**, 2159 (1969); *Progr. Theor. Phys.*, **39**, 1326 (1968).

([26]) J. BELL and E. DE RAFAEL: *Nucl. Phys.*, **11** B, 611 (1969).

([27]) S. J. BRODSKY and J. D. SULLIVAN: *Phys. Rev.*, **156**, 1644 (1967); T. BURNETT and M. J. LEVINE: *Phys. Lett.*, **24** B, 467 (1967).

an effort to eliminate the divergences in QED, and partly in order to understand the $\mu - e$ mass difference. A list of the different cases for which the modification Δa to the anomalous moment has been calculated is given by BAILEY and PICASSO ([15]). We mention here some of the principal conclusions, all to two standard deviations (95% confidence), assuming that each effect is operating alone and that there are no accidental cancellations:

i) A conventional cut-off ([28]) for the photon propagator at high q^2, or negative metric photons ([29]), would lower the theoretical result by $\Delta a/a = -2m_\mu^2/3\Lambda^2$, making the discrepancy in eq. (24) greater and implying $\Lambda > 5$ GeV.

ii) Similarly, if an arbitrary form factor ([30]) is applied to the muon vertex, $F(q^2) = (1 - q^2/\Lambda^2)^{-1}$, we require $\Lambda > 7$ GeV.

iii) The experiment puts limits on new fields ([31]) coupled to the muon. For example, for a vector field of mass M with coupling constant $f^2 \equiv g^2/4\pi$, $\Delta g/g = (1/3\pi)(f^2/M^2)m_\mu^2$ implying $f^2/M^2 < 6 \cdot 10^{-4}/M_N^2$, where M_N is the nucleon mass.

iv) If fermions exist with mass m_λ intermediate between electron and muon, then corresponding loops must be inserted in the photon propagator of the second-order diagram leading to an increase ([32]) in a_{theory}. From the absence of this effect it follows that $m_\lambda/m_e \geqslant 32$ (95% confidence), and $\geqslant 50$ (65% confidence).

8. – Lifetime of the muon in flight.

The theoretical value of the muon lifetime is calculated from the lifetime at rest ([33]) with the standard relativistic time-dilation obtained from the

---

([28]) V. B. BERESTETSKY, O. N. KROKHIN and A. K. KHLEBNIKOV: *Žurn. Èksp. Teor. Phys.*, **30**, 788 (1956) (English translation in *Sov. Phys. JETP*, **12**, 993 (1961)).

([29]) T. D. LEE and G. C. WICK: *Nucl. Phys.*, **9** B, 209 (1969); **10** B, 1 (1969).

([30]) B. DE TOLLIS: *Nuovo Cimento*, **16**, 203 (1960).

([31]) J. SCHWINGER: *Ann. of Phys.*, **2**, 407 (1957); I. YU. KOBZAREV and L. B. OKUN': *Žurn. Èksp. Teor. Fiz.*, **41**, 1205 (1961) (English translation: *Sov. Phys. JETP*, **14**, 859 (1962)); S. NAKAMURA, H. MATSUMOTO, N. NAKAZAWA and U. UGAI: *Suppl. Progr. Theor. Phys.*, extra number, 422 (1968); S. J. BRODSKY and E. DE RAFAEL: *Phys. Rev.*, **168**, 1620 (1968); R. SUGANO: *Progr. Theor. Phys.*, **28**, 508 (1962); K. M. CASE: *Phys. Rev.*, **76**, 1 (1949).

([32]) This remark was made by J. S. BELL: private communication. We are grateful to P. GODDARD and L. M. LEDERMAN, and independently to P. K. KABIR, for evaluations of the integral (ref. ([17])) giving the vacuum polarization as a function of the ratio (m_λ/m_μ).

([33]) See, for example, G. FEINBERG and L. M. LEDERMAN: *Ann. Rev. Nucl. Sci.*, **13**, 466 (1963).

known magnetic field and the mean radius as determined by the rotation frequency:

$$\gamma \equiv (1 - v^2/c^2)^{-\frac{1}{2}} = \lambda(1 + a)^{-1}(\bar{\omega}_p/\omega_{rot}) , \tag{25}$$

the overall error in τ_{th} being $\pm 0.15\,\%$. Here it is assumed that no special correction is necessary when the orbit is deflected by a magnetic field, and that the decay rate of the particle in its rest system is not altered by the acceleration experienced.

The lifetimes obtained from the maximum likelihood fit to the data for the individual runs are given in Table IV. Comparing with theory we find for the weighted mean

$$\tau_{exp} - \tau_{theory} = -(0.30 \pm 0.03)\ \mu s = (-1.1 \pm 0.1)\,\% . \tag{26}$$

We interpret this as evidence for a slow loss of muons from the ring due to a gradual blow-up of the beam excited by small irregularities in the magnetic field. A computer simulation, in which we follow particles by means of a step-by-step integration in the measured magnetic field over many turns, shows losses of the same order. A similar result is obtained if the orbit stability is analysed with the Schoch theory ([34]). Further details are given in Appendix C.

Whether these losses exist or not, eq. (26) shows that the time dilation of special relativity is verified to within 1.1 % for $\gamma = 12$. It is emphasized that this experiment involves muons travelling in a circular orbit, simulating the out-and-return journey often discussed ([35]) in connection with the twin paradox. This result removes any lingering suspicion that some unsuspected effect associated with acceleration would compensate the time dilation in a circular or out-and-return journey; the *clock-paradox* is established as an experimental fact associated with the time keeping of radioactive material in direct comparison with standard laboratory time scales. Several indirect checks of the relativistic transformation of time in accelerated motion, at at somewhat lower velocities, have already been established ([36]). Unpublished evidence for muon time dilation in circular orbits at $\gamma \sim 1.2$ was also obtained by CHARPAK *et al.* ([1]) in an earlier $(g-2)$ measurement at CERN, and the interpretation of the experiment has been further discussed by BAILEY and PICASSO ([15]).

([34]) A. SCHOCH: *The Theory of Linear and Nonlinear Perturbations of Betatron Oscillations in Alternating Gradient Synchrotrons* (Geneva, 1957), CERN 57-21.

([35]) A. EINSTEIN: *Ann. der Phys.*, **17**, 89 (1905); H. BONDI: *Discovery*, **18**, 505 (1957); R. P. FEYNMAN, R. B. LEIGHTON and M. SANDS: *The Feynman Lectures on Physics*, Vol. **1**, Sect. **16**.2 (London, 1964).

([36]) R. V. POUND and G. A. REBKA jr.: *Phys. Rev. Lett.*, **4**, 274 (1960); C. W. SHERWIN: *Phys. Rev.*, **120**, 17 (1960).

* * *

We thank the many colleagues at CERN whose collaboration made this experiment possible. In particular, we would like to thank L. M. LEDERMANN and M. TANNENBAUM for their participation in part of the experiment and for stimulating discussions.

I. PIZER amd H. VERWEIJ have contributed to the design of the digitron and, together with M. MOORE, have taken care of its construction and running in.

We also thank J. LINDSAY, P. CROSSLAND, F. ISELIN and F. PONTING, who worked on the design and setting up of our special electronics equipment.

We appreciated very much the excellent technical support provided by H. ANCEY, E. BALTZERZEN, G. FRÉMONT, E. FRICK, G. GRIOT, K. MUHLEMANN and H. WARREN.

We wish to thank B. KUIPER for setting up the PS fast ejection to suit our requirements and the PS operators for keeping it well tuned.

Finally, we wish to acknowledge the contribution by the University of Munich of an on-line computer.

APPENDIX A

Detailed calculation of the muon intensity.

A·1. *The stored muon intensity* (*). – The muon capture yield per available proton of given energy will be a function of the method of injection and of the ring parameters. These are: the semi-aperture of the storage region (a) in the horizontal plane, b) in the vertical one), the radius of the ring ϱ, the magnetic field B, and the field index n.

It is difficult to express the influence of all these parameters in a general formula. However, for a given injection system and inside a limited range of the parameters, one can accept the following expression:

$$Y_\mu = f \cdot \frac{ba^3}{\varrho^4} \cdot n^{\frac{1}{2}}(1-n)^{\frac{1}{2}} \cdot p_\pi \cdot Y_\pi = f_1 \cdot \frac{ba^3}{\varrho^3} \cdot n^{\frac{1}{2}}(1-n)^{\frac{1}{2}} B \cdot Y_\pi \,, \tag{A.1}$$

where Y_μ is the muon capture yield; Y_π is the yield of pion production (per GeV/c and steradian)—which is a function of the proton and the pion momenta; and f or f_1 are factors depending on the chosen injection system.

The expression given above can be explained as the product of the angular acceptance in the vertical plane $(b/\varrho)\, n^{\frac{1}{2}}$, the angular acceptance in the hori-

(*) We are indebted to F. COMBLEY, G. PETRUCCI and W. WORDEN who contributed, at different stages of the experiment, to our understanding of the injection mechanism. In particular F. COMBLEY wrote part of this Appendix.

zontal plane $(a/\varrho)(1-n)^{\frac{1}{2}}$, the momentum bite of the pion $(a/\varrho)p_\pi(1-n)$, and finally the acceptable fraction of the muon momentum spectrum $\sim a/\varrho(1-n)$.

In f, f_1 the decay probability of the pions and the losses due to the $\pi\mu$ decay angle must be included; in fact these losses might be rather high when the angular acceptances of the ring are comparable to the decay angles.

A·2. *Calculation of trapping efficiency.* – A computer program is used to calculate the number of captured muons properly. The program starts with a given pion source distribution (in vertical and horizontal phase-space, and momentum), and calculates the trapping efficiency for muons as a function of pion momentum and horizontal injection angle. Together with the stored muon intensity, the program calculates the radial and longitudinal polarizations of the muon, and how far the pions go before hitting something.

A·3. *Phase-space representation.* – In a weak-focusing field, consisting only of dipole and quadrupole terms, the trajectory of any particle can be represented as a circle in phase if the vertical scale factor is chosen appropriately. The complete turn corresponds to one betatron oscillation in the focusing ring. Examples of this representation in horizontal and vertical phase-space are shown in Fig. 24.

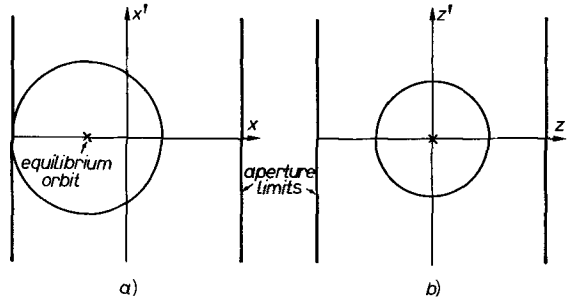

Fig. 24. – In a weak-focusing field the trajectory of any particle can be represented as a circle in phase space, if the vertical scale factor is chosen appropriately. *a*) In the horizontal plane circles are centred on the x-axis at the position of the equilibrium orbit, *b*) in vertical plane circles are centred at the origin.

A·4. *Vertical phase-space.* – The region of acceptance of the stored muons is represented by a circle with its centre at the origin and with radius equal to the semi-aperture. In order to produce a stored muon, a pion must decay when the point representing its motion in vertical phase-space lies within the above cirlce. To simplify the calculation, the muon circle has been displaced on the angular axis by a distance equal to the vertical $\pi\mu$ decay angle.

In vertical phase-space, the pions are initially uniformly distributed along a line representing the target. As the injected pions travel round the ring, so the pion distribution in vertical phase-space rotates. Each point representing a pion moves on a circle; the pion is lost if the circle intersects the aperture limits. At a given time, the number of pions that can give stored muons is proportional to the length of the line representing the pion source

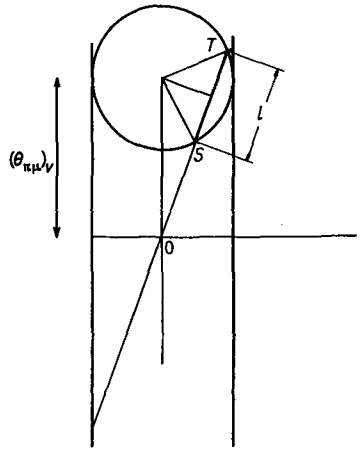

Fig. 25. – At a given time, the pions are distributed in vertical phase space along the line OT. The circle, which represents the vertical acceptance region of the stored muon, is displaced vertically by θ_v (vertical decay angle).

(see Fig. 25). This factor, together with the decay probability, is used to determine the muon birth rate as a function of time and vertical decay angle. To obtain the number of stored muons, the muon birth-rate is integrated between the limits set by the trajectories in horizontal phase-space (see below).

A·5. *Horizontal phase-space.* – The pion trajectories originate from a line-source distribution, as indicated in Fig. 26; they are defined by the pion momentum (which gives the position of the equilibrium orbit), and by the angle of injection. Therefore, in horizontal phase-space the trajectories of the

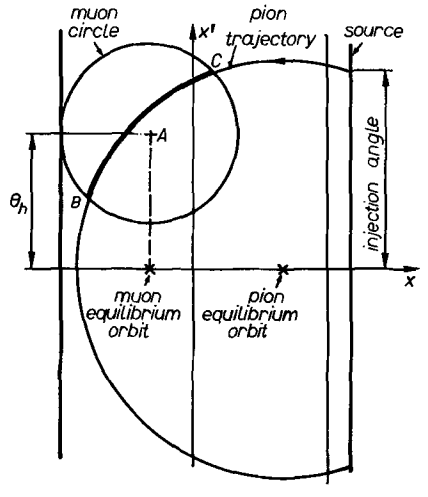

Fig. 26. – In horizontal phase-space a pion trajectory originates from a line-source distribution; it is defined by the pion momentum and by the angle of injection. A pion can give a stored muon of momentum p_μ only when it is within the displaced circle, which represents the horizontal acceptance region of the stored muons displaced vertically by θ_h (horizontal decay angle).

injected pions are represented by circles centred at the position of their equilibrium orbit; this position is not restricted to within the aperture limits, although the pion is considered lost at the point where its trajectory crosses the boundary limits of the aperture. The region accessible to muons of a given momentum is represented by another circle, tangential to the geometrical limits of the storage region. Referring to Fig. 26, we see that a pion produced at the target with a momentum p_π and an injection angle x'_π can decay with a horizontal decay angle θ_h to give a stored muon of momentum p_μ only when it is within the circle, which represents the acceptance region of the stored muons displaced vertically by θ_h. The heavy line shows the part common to the pion trajectory and the muon acceptance. The two points C and B on the pion trajectory represent the two points in time between which the muon birth-rate is to be integrated. Some pions may complete more than one horizontal betatron oscillation and so pass through the muon circle again. In this case, the integration has to be repeated over these later time intervals.

So far, to explain the main line of the program, it has been assumed that the trajectories of pions in phase-space are circles. However, this assumption is only true for particles of given momentum, and the scale factor has been chosen so that particles with equilibrium orbits in the centre of the storage region move in a circle. The approximation that the trajectories of pions are given by circles in phase-space is not good for particles with momentum that is more than 10 % larger than the momentum of the stored muons at the centre of the aperture. It can be shown that in general a trajectory can, in both horizontal and vertical phase-space, be represented by an ellipse. In the program used to evaluate the stored muon intensity, the corrected pion trajectories in phase-space have been considered.

A·6. *Calculation of polarization.* – The $\pi\mu$ decay angle is determined by the pion and muon momenta, but the orientation of the decay plane about the pion momentum vector is random. If we denote this orientation by ψ, then the horizontal (θ_h) and vertical (θ_v) components of the decay angle are given by

$$\theta_h = \theta \cos \psi \tag{A.2}$$

and

$$\theta_v = \theta \sin \psi \,, \tag{A.3}$$

where θ is the angle between the pion and muon momenta in the laboratory.

The initial angle between the muon spin and momentum is expressed as the difference between the rest-frame (pion) and laboratory-frame decay angles. The initial longitudinal polarization is therefore the cosine of this angle and the initial radial polarization is the sine multiplied by $\cos \psi$. The positive direction for radial polarization is towards the centre of the ring.

A·7. *Resumé of basic formulae used in the stored muon intensity program.*

A·7.1. For the ring. Betatron wavelength:

$$\lambda_H = 2\pi\varrho(1-n)^{-\frac{1}{2}} \simeq \frac{2\pi}{0.3B} p(1-n)^{-\frac{1}{2}} \,, \qquad (p \text{ in GeV/c}, \; B \text{ in Wb/m}^2) \,, \tag{A.4}$$

$$\lambda_V = 2\pi\varrho n^{-\frac{1}{2}} \simeq \frac{2\pi}{0.3B} p n^{-\frac{1}{2}} \,, \qquad (p \text{ in GeV/c}, \; B \text{ in Wb/m}^2) \,. \tag{A.5}$$

Equilibrium orbit:

$$\frac{\Delta\varrho}{\varrho_0} = \frac{\Delta p}{p_0}(1-n)^{-1}. \tag{A.6}$$

Angular acceptance of the ring:

$$\dot{x}_{\max} = \pm a(\lambda_H/2\pi)^{-1}, \tag{A.7}$$

$$\dot{y}_{\max} = \pm b(\lambda_V/2\pi)^{-1}, \tag{A.8}$$

a and b being the semi-apertures, horizontal and vertical, of the chamber.

A'7.2. For the kinematics of $\pi\mu$ decay.

$$\begin{cases} p^* \simeq 30 \text{ MeV}/c, \\ p_\mu \simeq p_\pi(0.79 + 0.21\cos\theta^*), \end{cases} \tag{A.9}$$

pion mass = 139.6 MeV, muon mass = 105.6 MeV.

The decay distribution being isotropic in the centre of mass of the pions, the probability of decay is constant as a function of $\cos\theta^*$, and the differential momentum spectrum of the muon is flat. The probability of decay inside the momentum bite Δp_μ is then

$$\Delta f = \frac{\Delta p_\mu}{0.42 p_\pi} \tag{A.10}$$

for $0.58 p_\pi \leqslant p_\mu \leqslant p_\pi$ (otherwise $\Delta f = 0$).

A'7.3. For the polarization of the stored muon beam. The radial polarization (P_r) of the muon is defined to be the component of its spin transverse to its laboratory velocity, as measured in its rest frame, or

$$P_r = \frac{\gamma_\pi \beta_\pi \sin\theta^*}{\gamma_\mu \beta_\mu}, \tag{A.11}$$

where θ^* is the muon angle in the pion rest frame, $\gamma_\pi = E_\pi/m_\pi$ and β_μ is the muon velocity in the laboratory. Expressed in terms of laboratory quantities, the above formula becomes

$$P_r = \frac{\sin\theta}{\sin\theta_{\max}}, \tag{A.12}$$

where θ is the muon laboratory angle and $\theta_{\max}$ its maximum laboratory angle:

$$\theta_{\max} = \arcsin\left\{\frac{(m_\pi^2 - m_\mu^2)}{2 p_\pi m_\mu}\right\} \tag{A.13}$$

(p_π is the pion momentum).

The longitudinal polarization of the muon is the component of its spin along the direction of its motion, measured in its rest frame, or

$$P_l = \frac{u - [(m_\mu^2/m_\pi^2)(1-u)]}{u + [(m_\mu^2/m_\pi^2)(1-u)]} . \tag{A.14}$$

The paramater u is defined by the following relation:

$$u = (E_\mu - E_{\min})/(E_{\max} - E_{\min}) = \cos^2(\theta^*/2) ,$$

where E_μ is the muon energy in the laboratory,

$$E_{\min} \simeq \frac{m_\mu^2}{m_\pi^2} E_\pi = 0.58 E_\pi \qquad \text{for } \theta^* = \pi$$

and

$$E_{\max} \simeq E_\pi \qquad \text{for } \theta^* = 0 .$$

APPENDIX B

Trajectories of electrons from muon decay in the ring.

The program takes muon decays at particular azimuthal positions, but the radial position and decay angles are chosen at random, weighted according to their expected distributions. If the electrons have an energy greater than some minimum energy, they are tracked out of the ring step by step until they reach a specified radius.

Consider an electron emitted in the muon rest frame at angle Θ^* to the direction of the muon in the laboratory frame, and with a momentum

$$x = p_e^*/p_{e,\max}^* . \tag{B.1}$$

The values of x are weighted according to the spectral function $n(x)$. Actually, one has

$$n(x)\,\mathrm{d}x = 2x^2(3-2x)\,\mathrm{d}x . \tag{B.2}$$

After having generated a value of electron momentum in the muon rest frame according to eq. (B.2), one computes the electron momentum p_e in the laboratory frame:

$$p_e = f(x, \cos\Theta^*) . \tag{B.3}$$

Equations (1), (2) and (3) specify the motion of the electron in the muon rest frame and in the laboratory frame. The laboratory emission angle of the

electron Θ is given by

$$\text{(B.4)} \qquad \operatorname{tg}\Theta = \frac{1}{\gamma_\mu}\,\frac{\sin\Theta^*}{\beta_\mu/\beta_e^* + \cos\Theta^*}\,.$$

The values of $\cos\Theta^*$ are chosen at random in the range $+1$ to -1.

The azimuthal angle of the decay φ is chosen at random in the range between 0 and π radians (see Fig. 27). Then the final emission angles of the electron in the horizontal plane (u) and in the vertical plane (v) are given by the following:

$$\text{(B.5)} \qquad \operatorname{tg} u = \operatorname{tg}\Theta \sin\varphi\,,$$

$$\text{(B.6)} \qquad \operatorname{tg} v = \operatorname{tg}\Theta \cos\varphi \cos u\,.$$

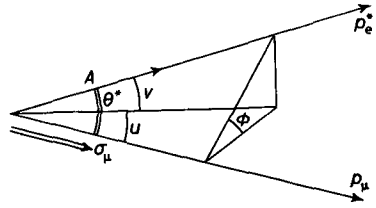

Fig. 27. – Direction of the decay electron momentum in the muon rest frame and that of the momentum in the laboratory frame. The azimuthal angle of the decay φ is chosen at random in the range between 0 and π radians.

The set of relations that we have written specifies the electron momentum and the emission angles in the laboratory as functions of three random variables (the spectral function, the zenith angle and the azimuth angle in the muon rest frame). We then compute the electron trajectories, taking into account the horizontal and vertical distributions of muons.

The radial and vertical positions of the muons follow a cosine distribution law if we take into account the betatron oscillations around their equilibrium orbits.

The magnetic field gradient has been considered constant ($n = 0.13$) through all the muon storage ring aperture, but a fringing field has been put in to compute the motion, both in the horizontal and vertical directions, of the decay electrons leaving the storage ring.

Until now the electron emission has been treated as isotropic. It remains to compute, for the particles falling in a particular energy angle box, the average asymmetry coefficient, and the muon-spin angle corresponding to the maximum intensity.

Suppose the muon spin direction is specified by unit vector $\hat{k}$. The intensity of emitting an electron in any direction $\hat{k}$ can be written

$$\text{(B.7)} \qquad I = 1 + \boldsymbol{A}\cdot\hat{\boldsymbol{k}}\,,$$

where $\boldsymbol{A}$ is the *asymmetry vector* of length equal to the asymmetry coefficient, which is a function of the electron energy in the muon rest frame, and direc-

tion parallel to the electron emission Θ^* considered. Over m decays the average intensity is therefore

$$\bar{I} = 1 + \frac{1}{m}\sum_{i=1}^{m} \boldsymbol{A}_i \cdot \hat{\boldsymbol{k}} = 1 + \bar{\boldsymbol{A}} \cdot \hat{\boldsymbol{k}} \,. \tag{B.8}$$

The quantity $\bar{\boldsymbol{A}}$ is the vector average of the individual asymmetry vectors $\boldsymbol{A}_i$. The modulus $|\bar{\boldsymbol{A}}|$ determines the mean asymmetry coefficient for any group of decays. The condition $\hat{\boldsymbol{k}} \| \bar{\boldsymbol{A}}$ determines the spin direction which gives a maximum counting rate for this group. In computing $\bar{\boldsymbol{A}}$ we sum up the horizontal projections of each $\boldsymbol{A}_i$, parallel and perpendicular to the muon velocity. The individual asymmetry coefficient $|\boldsymbol{A}_i|$ is a function of $x_i = (p_e^*/p_{e,\max}^*)_i$:

$$A_i(x) = |\boldsymbol{A}_i| = \frac{2x_i - 1}{3 - 2x_i} \,. \tag{B.9}$$

The components of $\boldsymbol{A}_i$ in the horizontal plane are given by the following relations:

$$\begin{cases} (A_i)_\parallel = A_i(x) \cos \Theta^* \,, \\ (A_i)_\perp = A_i(x) \sin \Theta^* \cos \varphi \,. \end{cases} \tag{B.10}$$

The component of $\boldsymbol{A}_i$ perpendicular to the median plane is given by

$$(A_i)_v = A_i(x) \sin \Theta^* \sin \varphi \,. \tag{B.11}$$

Being interested only in an effective value of A_i: $(A_i)_{\text{eff}}^2 = (A_i)_\parallel^2 + (A_i)_\perp^2$, we determine the average asymmetry coefficient A_{eff} for m decays going into a particular energy-angle box in the laboratory frame:

$$A_{\text{eff}} = \frac{1}{m}\left[\left(\sum_{i=1}^{m} A_i(x) \cos \Theta^*\right)^2 + \left(\sum_{i=1}^{m} A_i(x) \sin \Theta^* \cos \varphi\right)^2\right]^{\frac{1}{2}} . \tag{B.12}$$

The muon spin angle Θ_{eff}^* which corresponds to the maximum intensity is given by

$$\Theta_{\text{eff}}^* = \text{tg}^{-1}\left\{\frac{\sum A_i(x) \sin \Theta^* \cos \varphi}{\sum A_i(x) \cos \Theta^*}\right\} . \tag{B.13}$$

In Table VIII we give a typical output showing the number of decays *vs.* the laboratory electron energy and the angle of emergence. In Table IX we give an output showing the asymmetry coefficient A_{eff} *vs.* the laboratory electron energy and the angle of emergence. These results have been obtained by following $5 \cdot 10^4$ decay electrons. It is possible that electrons produced at certain angles and energies in the laboratory frame may be lost; in fact the field tends to bend the electrons inwards towards the counters, so that electrons emitted outwards from the ring are still detected, but some others may be lost due to vertical defocusing.

About 50% of the decay electrons hit the magnet poles and are lost.

TABLE VIII. – *Number of decay electrons incident on the counters.*

Angle of emergence from the ring ↓ / → Energy (MeV)							
0	0	0	0	0	0	0	0
0	0	0	0	0	0	0	0
0	0	0	0	0	0	0	0
0	0	0	0	1	34	127	242
11	92	195	316	492	460	386	196
576	521	369	206	60	1	0	0
117	10	0	0	0	0	0	0

Energy interval 60 MeV, maximum energy 1.14 GeV.

TABLE IX. – *Asymmetry coefficient* $A_{\text{eff}} \cdot 10^{-4}$.

Angle of emergence from the ring ↓ / → Energy (MeV)								
0	0	0	0	0	0	0	0	0
0	0	0	0	0	0	0	0	0
0	0	0	0	0	0	0	0	0
0	0	0	0	1967	2048	2401	2836	3141
593	1172	1316	1571	1839	2166	2547	2772	3109
981	1079	1371	1711	2022	9933	0	0	0
1026	3730	0	0	0	0	0	0	0

Energy interval 60 MeV, maximum energy 1.14 GeV.

About $5 \cdot 10^{-4}$ of them will be stored in the ring; owing to synchrotron radiation they will spiral inwards.

The geometrical efficiency varies with the energy and the angle of emergence of the electron. The horizontal aperture was divided into four regions, each of 2 cm horizontal width, made up of two equally populated strips of 1 cm width. The vertical distribution in each case is the usual cosine distribution. The variation of the efficiency in terms of NA^2 from the inside to the outside regions is about 20 %.

APPENDIX C

Calculations of muon losses due to beam blow-up.

Small imperfections in the magnetic field of the storage ring and variations of the magnetic field can cause particle losses due to gradual blow-up of the

									rad
0	0	0	0	0	0	0	0	62	0.05
0	0	0	0	0	16	116	101	119	0.10
16	123	231	257	217	140	60	1	0	0.15
278	214	80	0	0	0	0	0	0	0.20
0	0	0	0	0	0	0	0	0	0.25
0	0	0	0	0	0	0	0	0	0.30
0	0	0	0	0	0	0	0	0	0.35

								Total	rad
0	0	0	0	0	0	0	8865	8865	0.05
0	0	0	0	6378	6740	7303	8012	7312	0.10
4286	4718	5201	5648	6129	6676	7955	0	5265	0.15
4314	4583	6105	0	0	0	0	0	3426	0.20
0	0	0	0	0	0	0	0	2024	0.25
0	0	0	0	0	0	0	0	1022	0.30
0	0	0	0	0	0	0	0	383	0.35

beam. Two methods have been used to study the trajectories of particles in the magnetic field of the storage ring.

C'1. *Particle tracing.* – This method ([10]) is a computer simulation in which we follow particles by means of a step-by-step integration of the equation of motion over many turns. The method is to analyse the sets of measured values of the total field B_0 and skew gradient $\mathrm{d}B_z/\mathrm{d}z$, at each of the 288 azimuthal measuring points in the field map. The analysis fits coefficients A_n, B_n, to a solution of the two-dimensional Laplace equation for a magnetic potential:

$$V = \sum_{n=1}^{5} (A_n r^n \sin n\varphi + B_n r^n \cos n\varphi) \,. \tag{C.1}$$

From these coefficients the field at any point in the magnet aperture may be calculated, with precision up to decupole components of the field for $n = 5$.

The equations of motion of the particle in the magnetic field are now integrated stepwise by the Runge-Kutte method, substituting, at each step,

field values calculated from the coefficients of the field. In this manner it is possible to study nonlinear oscillations of the particle trajectories in the measured magnetic field. By Monte Carlo methods we *inject* a population of particles into this model of the field in order to study beam blow-up and losses due to resonance. We conclude from these studies that:

i) Due to beam losses, the stored beam intensity after 100 orbits is only 80% of that expected from a conservative calculation of the magnet acceptance.

ii) There is no significant radial asymmetry in the beam losses.

iii) Beam losses after 100 turns appear to be small. Resonance oscillation amplitudes appear to reach a stable level after a few hundred turns; slow, continuous blow-up has not been observed.

Using the same particle tracing technique we have examined the time-averaged field experienced by a particle executing betatron oscillations about either circular or noncircular closed orbits in a nonuniform field. Averaging over a Monte Carlo injected population of particles representing the real population of the storage ring, we find that the mean time-averaged field is 29 ppm higher than the mean field measured around a circular orbit at the mean radius of the particle population. This time-averaged field shift must therefore be applied to the fields measured on circular orbits as tabulated in the field maps.

(If the program is set to calculate field shifts for particles oscillating about circular equilibrium orbits, the resulting shift is in agreement with analytical calculations.)

C'2. *Resonance analysis.* – The efficiency of the particle-tracing method is not very high for investigating particle losses at times later than 100 turns. We used a second method to study muon losses at later times ([37]) by analysing the stability of the betatron motion of particles in terms of a formalism proposed earlier by SCHOCH ([34]).

Resonances of the betratron motion of particles in a storage ring occur if a resonance condition

$$aQ_x + bQ_z = c \tag{C.2}$$

is fulfilled. The numbers a, b, c are integers, and Q_x and Q_z are the numbers, of betatron oscillations per revolution for the horizontal and the vertical motion.

If the condition (C.2) is satisfied, small imperfections of the magnetic field of the storage ring can induce large variations of the betatron amplitude. Figure 28 represents the resonance lines up to the fifth order in the (Q_x, Q_z)-plane. In the muon storage ring, the field index lies between 0.10 and 0.15.

We use the analysis of the magnetic field of eq. (C.1) and determine, for each resonance separately, the amount of particle losses it can produce. In general, resonances of higher order $N = a + b$ (with a and b as from eq. (C.2)) are less dangerous. Taking into account the muon distribution in the storage

([37]) G. VON BOCHMANN: Diplom-Thesis at Lehrstuhl, Prof. MEYER-BERKHOUT, University of Munich (1968).

ring and the variation of the field index with the radius, we find that the largest contribution to the losses of muons more than 100 turns is due to the fourth-order resonance $Q_x + 3Q_z = 2$, the influence of the other resonances being comparably small.

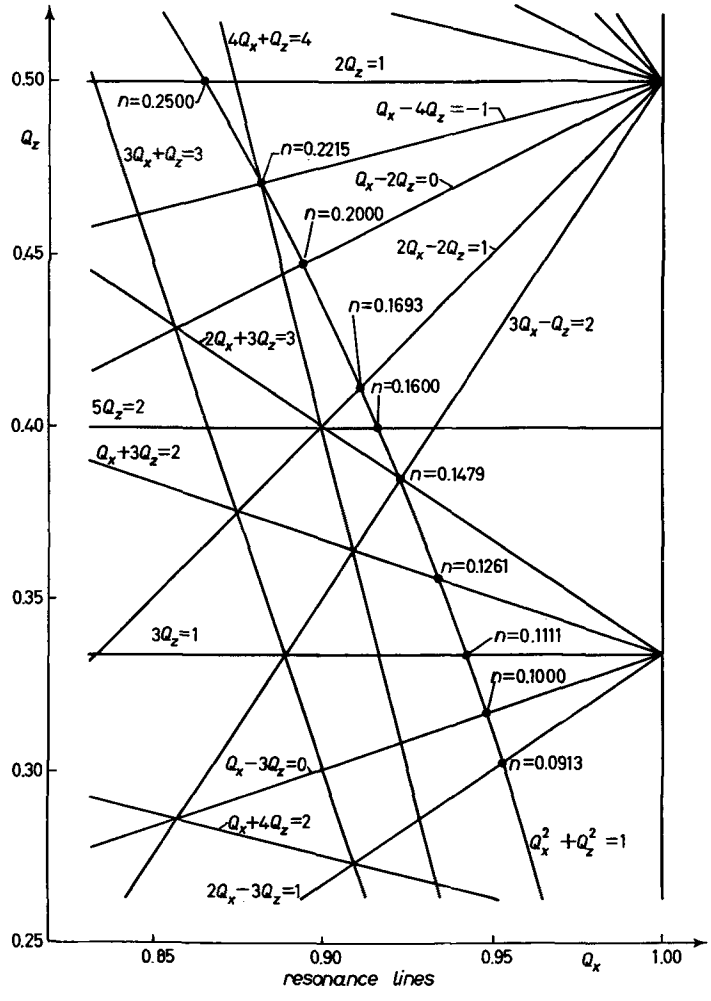

Fig. 28. – Resonance lines up to the fifth order in the (Q_x, Q_z) plane. In the muon storage ring the field index lies between 0.10 and 0.15.

There are two important approximations which enter into the resonance analysis of muon losses:

i) only long-term stability is considered (losses after 100 turns and more),

ii) we assume that the different resonances act independently.

We conclude from the resonance analysis that there are particle losses of $(4.0^{+4.0}_{-2.5})\%$ of the total intensity at times later than 5 μs (100 turns) and

losses of $(1.5^{+1.5}_{-1.0})\%$ at times later than 20 μs (400 turns). The error on these numbers is due to the uncertainties of the field coefficients that are responsible for exciting the resonance in question, and which are determined from the measured magnetic field map through the coefficients A_n and B_n of eq. (C.1).

● RIASSUNTO (*)

Si è misurato il momento magnetico anomalo $a \equiv \frac{1}{2}(g-2)$ del muone nell'anello di accumulazione di muoni del CERN. Il risultato è $(116\,616 \pm 31)\cdot 10^{-8}$ in confronto al valore teorico $(116\,588 \pm 2)\cdot 10^{-8}$ con un accordo di (240 ± 270) parti per milione. Si è trovato che la vita media dei muoni che si muovono su un'orbita circolare con $\gamma = 12$ concorda con la dilatazione del tempo predetta dalla relatività ristretta entro 1.1%. Si espongono i dettagli del magnete dell'anello di accumulazione, della strumentazione e dell'analisi dei dati. Si discutono le implicazioni teoriche dei risultati.

(*) *Traduzione a cura della Redazione.*

Точное измерение аномального магнитного момента мюона.

Резюме не получено.